Front page

Exam information
NFYA09004E - Nanoscience Thesis 60 ECTS, Niels Bohr Institute - Contract:134648 (Lukas Zeppelin)

Handed in by
Lukas Zeppelin
dzx335@alumni.ku.dk

Exam administrators
Eksamensteam, tel 35 33 64 57
eksamen@science.ku.dk

Assessors
Heloisa Nunes Bordallo
Examiner
bordallo@nbi.ku.dk
+4535321215

Esben Bryndt Klinkby
Co-examiner
esbe@dtu.dk

Hand-in information

Title: Inelastic Neutron Scattering Study of Thymol & para-Cymene as Potential Neutron-Moderating Materials
Title, english: Inelastic Neutron Scattering Study of Thymol & para-Cymene as Potential Neutron-Moderating Materials
The sworn statement: Yes
Does the hand-in contain confidential material: No

UNIVERSITY OF COPENHAGEN
FACULTY OF SCIENCE

Master Thesis

Inelastic Neutron Scattering Study of Thymol & para-Cymene as Potential Neutron-Moderating Materials

Author:
Lukas Zeppelin

Supervisor:
Heloisa Nunes Bordallo

Co-supervisor:
Svemir Rudić

May 21, 2023

Contents

Abstract

Neutron moderators can have many forms and sizes with water (H_2O), methane (CH_4) and molecular hydrogen (H_2) being the most commonly used moderating materials. These materials have very good neutron moderating characteristics, such as high proton density leading to favorable energy distributions of moderated neutrons, but they can have serious disadvantages as well. Solid methane is prone to radiolysis resulting in a variety of recombinant species, as well as gaseous hydrogen, which can damage the containing vessel. The H_2 moderator is currently only feasibly contained in liquid form at spallation type sources which ultimately leads to a broadened energy distribution of the moderated neutrons. As a result, the active search for new types of moderator materials, and especially cryogenic moderator materials, is underway around the world. This has led to the investigation of thymol ($C_{10}H_{14}O$), as well as para-cymene ($C_{10}H_{14}$), both hydrogen rich compounds. To better describe these hydrogenous molecules, inelastic neutron scattering (INS), Infrared and Raman spectra of thymol, as well as para-cymene were collected. The experimental data were then compared with theoretically derived vibrational frequencies calculated for the single molecule optimised geometries at the B3LYP/6-311++G(d,p) level of theory using Gaussian 16. Finally, the AbINS software, as implemented in Mantid, was used to simulate the INS spectra from the vibrational frequencies and the mean squared displacements of atoms from their equilibrium position. From the obtained results it was shown that both thymol and para-cymene possessed favorable, low energy, vibrational modes involving the rotation of their benze-bound methyl groups. These results suggested that both materials have favorable neutron moderating characteristics. As a conclusion it is emphasized that the glassy state of para-cymene should be analysed in more details.

1 Introduction

Neutrons are very different from other forms of probes that are used to study materials (photons, electrons) in that they have a mass but a neutral charge. This neutral charge means that they do not interact with the electrons surrounding the nucleus (whereas photons and electrons do), but predominantly with atomic nuclei [1].

A neutron left alone in a vacuum will have a neutron life time τ (the time after which $1/e = 0.37$ of the original population remains) and a half-life $t_{1/2}$ (the time taken for half of the populations of the neutrons to decay) of:

$$\tau = 885.7s$$

$$t_{1/2} = 613.0s$$

against its own decay $n \rightarrow p + e + \bar{v}_e$. Where p, e and $\bar{v}_e$ correspond to a proton, electron and an antineutrino, respectively [2], [3]. In most gases the neutron will be absorbed in a fraction of a second and for many solids it decays to a scale of milliseconds or even less.

The wave-like nature of the neutron means that the neutron with a given energy E_n has an associated de Broglie wavelength λ_n, and the two values are related with a well known relation [1]:

$$E_n = \frac{h^2}{2m_n\lambda_n^2} = \frac{\hbar^2 k_n^2}{2m_n} = k_B T \tag{1}$$

Here k_n is the wave vector and h is Planck's constant. The quantity of m_n is such that $\lambda_n \approx 2$ Å at $T \approx 300$ K. This wavelength is comparable to that of the interatomic spacing of solids and dense fluids making neutrons in this energy range fit for elastic scattering studies. The kinetic energy of neutrons in this temperature range are on the order of $E_k = 25$ meV, which is also on the same order of magnitude as other interatomic vibrational modes in solid-state systems. Thus, neutrons in the energy range of 25 meV, and their corresponding wavelengths, are fit for both elastic and inelastic studies of condensed matter systems.

Neutrons are produced through several methods, all of which involve some type of nuclear reaction. The most relevant nuclear reactions in the production of neutrons for use in scattering experiments, are spallation and fission. Spallation type sources, like the one at ISIS Neutron and Muon Source, start off by producing H^- ions (proton with two electrons). These negatively charged hydrogen ions are then accelerated by a linear accelerator (LINAC) and are stripped of electrons prior to being deposited into a storage ring (synchrotron) for further acceleration, as is the case at the ISIS Facility [4].

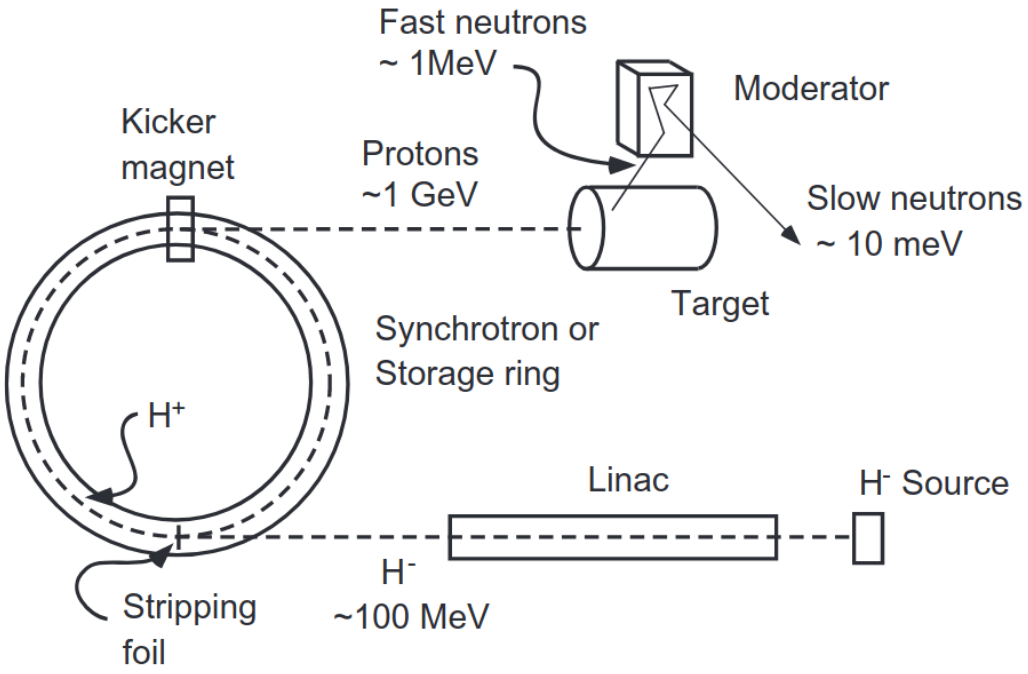

Figure 1: Schematic representation of a spallation type neutron source with a synchrotron [5].

Once the protons have been accelerated sufficiently into the GeV range, they are sent to impact on a target. The target is made up of elements rich in neutrons such as heavy elements and their isotopes. The nucleus of the target destabilizes due to the introduction of the proton and undergoes a number of different nuclear reactions that primarily release neutrons, but other particles are also released as a type of byproduct. The neutrons that are released from the nucleus in these processes have energy on the order of magnitude of several MeV and are not suitable for scattering experiments, yet. In order to bring these neutrons into the energy range needed for scattering experiments they need to be moderated. This whole process from proton, to neutron, to moderator neutron, is schematically illustrated in Figure 1.

The type of moderating material used is dependant on the energy scale of the physical properties that are being investigated. For elastic and inelastic scattering experiments light water moderators are commonly used to produce slow (thermal) neutrons.

The most prominent interaction found between matter and neutrons, and the most important when considering neutron moderation, is the simple elastic collision. Here an incident neutron bounces off of a nucleus where-after the nucleus recoils but remains in the same internal state, which is usually

the ground state.

After a neutron is scattered elastically away from a target of atomic weight M_A, the minimum final energy E_{min} of neutron with incident energy E_i is [6], [7]:

$$E_{min} = \left(\frac{M_A - 1}{M_A + 1}\right)^2 E_i \tag{2}$$

An ensemble of neutrons undergoing a scattering process according to the equation above will then be distributed between:

$$E_{min} \leq E_f \leq E_i \tag{3}$$

Where E_f denotes the final neutron energy.

Kinetic energy lost by the neutron is carried off as kinetic energy in the recoiling nucleus. On lighter nuclei, elastic collisions are the most probable process for neutrons with incident energies below several hundred keV. It is through this repeated scattering process while passing through matter that the neutron energy gets reduced, and thus moderated, until it reaches the thermal equilibrium of its surroundings.

A distribution of moderated neutrons follow a Maxwell-Boltzmann distribution and can span all the way from its original energy down to 5 meV or even lower. Many nuclei have internal excited states that span from a couple eV up to MeV. This implies is that, neutron energies in the keV range make it increasingly likely that the neutrons will scatter inelastically, exciting the recoiling nucleus. Another possibility is that the nucleus absorbs the neutron, thus resulting in a higher excited isotope of the incident nucleus.

Table 1 presents in-depth list of the various energy ranges than what is

Table 1: Common neutron wavelengths, velocities and energies, at various temperatures [8].

Temperature (K)	Wavelength (Å)	Velocity (m/s)	Energy (meV)
0.1 (Ultra-cold)	97.5	40	$8.6 \cdot 10^{-3}$
1	30.8	130	$8.6 \cdot 10^{-2}$
10	9.8	410	$8.6 \cdot 10^{-1}$
100	3.1	1280	8.6
300	1.8	2220	25
1000	1.0	4060	86

used in this thesis, where the focus is more on ultracold, cold, thermal and epithermal neutron energy ranges.

In the current state of neutronics cold and ultracold moderators are receiving a larger degree of attention due to their advantages in materials research. Liquid hydrogen (H_2), deuterium (D_2), and hydrocarbons, such as liquid or solid methane (CH_4), are the moderating materials of choice in accelerator based cold neutron sources [9]. Each material presents their set of advantages and disadvantages.

Molecular hydrogen comes in the form of two spin isomers; para (anti-parallel proton spin) and ortho (parallel proton spin) hydrogen, with para-hydrogen being preferable for cold neutron moderation due to para-hydrogen's energy dependant neutron scattering cross-section [10]. This presents a challenge since molecular hydrogen at ambient temperatures, so called normal-hydrogen, has a ortho to para ratio of 3:1 and needs cooling down to below 24 K for ortho to fully convert to the maximum value of 99% para-hydrogen [11]. This conversion process is very slow in the absence of any suitable catalyst and the back-conversion due to neutron irradiation is still relatively unknown [12].

Methane on the other hand serves as an alternative to hydrogen and has the benefit of a higher proton density of 0.079 protons/Å^3 at 20 K, compared to H_2 proton density of 0.042 protons/Å^3 at 20 K [11]. The main issue with methane moderators is that they are prone to radiolysis, yielding a number of different recombinant species such as carbon, various hydrocarbons as well

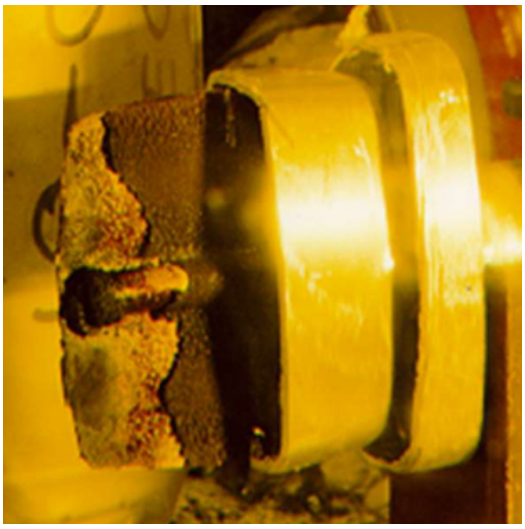

Figure 2: The build-up of 'carbon-like' deposits seen on a methane moderator [13].

as gaseous hydrogen (see Figure 2). This ultimately reduces the moderators efficacy with use as well as resulting in moderator breakdowns if the level of contaminants gets too high as has happened twice at the ISIS Facility [14], [15]. As a result the investigating of potential new moderating materials is underway and especially cryogenic moderating materials.

Mesitylene, (1,3,5-methylbenzene) and triphenylmethane (TPM) are materials which are already under study with mesitylene being proposed for use in compact accelerator driven sources [16], [17]. A cryogenic moderator based on a mesitylene mixture is already being utilized at the pulsed fast reactor IBR-2 in Dubna [18]. Mesitylene is found in 3 different solid phases with phase II, an amorphous disordered phase, being observed to be the best contender against liquid hydrogen. However, this compound is only superior to liquid hydrogen in the interval between 20 meV and 1 eV [19] and nowhere near as efficient as methane as a cold neutron source. Studies on TPM's moderating performance has not yet reached as far as mesitylene, but efforts have been made in characterising its VDoS as well as its temperature dependent total neutron scattering cross-section [17]. These efforts allow the construction of scattering kernels which are necessary for accurate Monte Carlo simulations on their neutron moderating capabilities. While these materials are already under investigation other possibilities are also being explored. This has lead to the investigation of thymol and para-cymene (p-cymene) as potential moderating materials. These materials have benzene backbones (see Figure 3), high proton densities, and are easily cooled to a solid state, thus increasing their proton densities. Thymol, also chemically known as 2-isopropyl-5-methylphenol, has been reported to possess a long

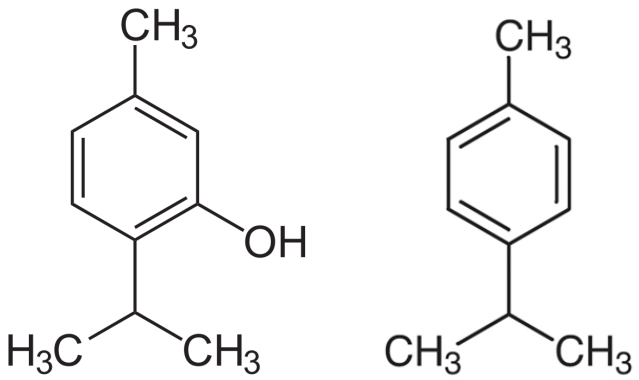

(a) **(b)**

Figure 3: Chemical structure of a) thymol ($C_{10}H_{14}O$) and b) p-cymene ($C_{10}H_{14}$) molecules.

Table 2: Boiling points and melting points of p-cymene, thymol, methane and hydrogen.

	Melting point (K)	Boiling point (K)
Thymol	322	322-324
p-Cymene	205	450
Mesitylene	228	438
Triphenylmethane	365-367	632
Hydrogen	14	20
Methane	91	112

list of medicinal properties, such as acting as an anti-inflammatory, analgesic, antibacterial and antiseptic, just to mention a few [20]. Thymol (see Figure 3a) has already presented itself useful in pharmacology. The chemical can be obtained from various readily accessible herbs, with *Thymus Vulgaris* containing the largest quantity of the compound.

Another compound p-cymene, also chemically known as 1-Methyl-4-(propan-2-yl)benzene, which can usually be extracted from the same materials as thymol, is almost structurally identical as thymol (Figure 3b), but lacks the OH-alcohol group on the benzene ring. p-Cymene shares similar pharmacological characteristics as thymol.

Both thymol and p-cymene contain a benzene back bone which provides resistance towards radiolysis. This hypothesis is based on previous studies of similar compounds also containing benzene backbones such as mesitylene, toluene and m-xylene. Where the release of hydrogen as the result of a neutron flux is 10 times lower than that of methane [17], [18]. Another desired feature of thymol and p-cymene are their melting- and boiling points (see Table 2). A major drawback of methane and hydrogen moderators are that they are in a gas-phase at room temperature, rendering maintenance on moderators using these materials tedious. This adds additional value to p-cymene and thymol as potential moderating materials as they are liquid and solid, respectively, at room temperatures which would significantly aid in maintenance of potential moderators incorporating these materials.

The quality of a cold moderator material is practically determined by its excitation spectrum because of how these excitations dominate in the energy exchange of neutrons at low temperatures [21]. This would indicate that the way to characterize the moderating capabilities of new compounds as potential neutron-moderating materials is to measure their vibrational density of states (VDoS). Therefore, the potential of utilizing thymol, p-cymene, or a combination of these compounds as moderators will be evaluated by analyz-

ing the experimental inelastic neutron scattering (INS) spectra, along with the theoretical INS spectra obtained through single molecule density functional theory (DFT) calculations. By combining these two methods, a solid foundation in characterizing these material's VDoS, and by extension their moderating capabilities, is possible. Furthermore, Fourier-transform infrared and Raman spectroscopic techniques have been carried out on these two materials with the intention of providing additional support in the characterization of VDoS, as well as verifying the efficiency of the single molecule DFT calculations from which the theoretical spectra are derived.

2 Theory

2.1 Slowing Neutrons Down

Elastic scattering is the simplest form of interaction between the neutron and the nucleus. Here the momentum of the system is conserved such that $E_i = E_f$ for the sum of the energy of the neutron and nucleus. In kinematic scattering between a neutron with mass $m_n = 1$ and a nucleus with mass M_A one can derive the relationship between the neutrons incoming energy E_i and final energy E_f as a function of the scattering angle θ [6], [7]:

$$\frac{E_f}{E_i} = \frac{M_A^2 + m_n^2 + 2M_A m_n cos(\theta)}{(M_A + m_n)^2} \approx \frac{M_A^2 + 1 + 2M_A cos(\theta)}{(M_A + 1)^2} \tag{4}$$

Eq. 4 has its minimum at a value of $M_A = 1$ (i.e. for hydrogen), where the backscattered ($\theta = 180°$) neutron loses all of its energy in a single collision. The average energy lost per collision is also an important quantity when investigating moderating capabilities of a new material [6], [22]:

$$< E_f > \approx \frac{1}{2} E_i \left(1 - \frac{1 + M_A^2 - 2M_A}{1 + M_A^2 + 2M_A}\right) = \frac{1}{2} E_i (1 - \alpha) \tag{5}$$

Where $\alpha = \left(\frac{M_A - 1}{M_A + 1}\right)^2$. This equation also shows that hydrogen exhibits the largest average energy transfer of any nucleus with $< E_{f,H} >= \frac{1}{2} E_i$, where $< E_{f,H} >$ is the average final output energy of an incident neutron scattered off of a hydrogen atom.

Another important quantity, the logarithmic energy decrement per collision $\xi =< ln(E_i) - ln(E_f) >$ [7], [23] :

$$\xi = 1 - \frac{(M_A - 1)^2}{2M_A} ln\left(\frac{M_A + 1}{M_A - 1}\right) \tag{6}$$

which is constant for a given nucleus, but can be calculated for entire molecules by averaging over all the nuclei, weighted by the scattering cross-section σ_s.

The average number of collisions, N, needed to slow a neutron produced from a target from its initial neutron energy labelled E_{target} (typically in the MeV range), to its cold and moderated energy $E_{moderated}$ (typically < 5 meV) can be calculated from ξ [24]:

$$N = \frac{ln(E_{target}) - ln(E_{moderated})}{\xi} \tag{7}$$

The energy decrement ξ, as well as the number of collisions necessary for cold moderation, for some common nuclei are presented in Table 3. Table 3

Table 3: Moderator values for nuclei found in common moderating materials.

	Hydrogen	Deuterium	Carbon	Oxygen
Mass (amu)	1	2	12	16
σ_{total} (barn*)	82.030	7.640	5.559	4.232
σ_{abs} (barn)	0.33	$5.20 \cdot 10^{-4}$	$3.52 \cdot 10^{-3}$	10^{-4}
Energy decrement (ξ)	1.000	0.725	0.158	0.120
N (1 MeV $\longrightarrow$ 5 meV)	~19	~26	~121	~159

Estimated values calculated from Eqs. 6 and 7. Total cross-section σ_{total} and absorption cross-section σ_{abs} (for 2200 m/s neutrons) values were taken from reference [25].
*barn is a standard unit of measurement used in nuclear physics and it is equal to 10^{-28} m^2 (100 fm^2).

indicates why hydrogenous materials are preferable for moderation in general, and especially for cold moderation. The number of collisions required for moderation are far fewer, thus requiring smaller moderator volumes. This ultimately reduces the chance of a neutron being absorbed by the moderating material, which would in turn reduce the final neutron flux.

It is important to highlight the benefit of deuterated moderating materials due to deuterium's low absorption cross-section, one of hydrogens largest caveats. For reactor based sources deuterium, and deuterated water, are the materials of choice as all they require are larger moderator volumes to counteract the smaller scattering cross-section, and both provide superior flux when compared to ^{1}H and light water. However, for pulsed type sources deuterium is not applicable as the larger volumes, as well as the increased scattering events required for moderation, leads to pulse broadening which ultimately reduces the resolution of the instruments that depend on the time-of-flight (TOF) calculations to operate [26]. This especially becomes an issue with cold moderation as the neutrons velocity are much lower thus further spreading the distribution of neutrons with respect to time [27].

2.2 Neutron Energy Distributions

The slowing down of neutrons, as described in previous section, is a purely classic mechanical description. However, if one is to imagine the distribution of neutron energies of neutron's exiting the moderator, a thermodynamic

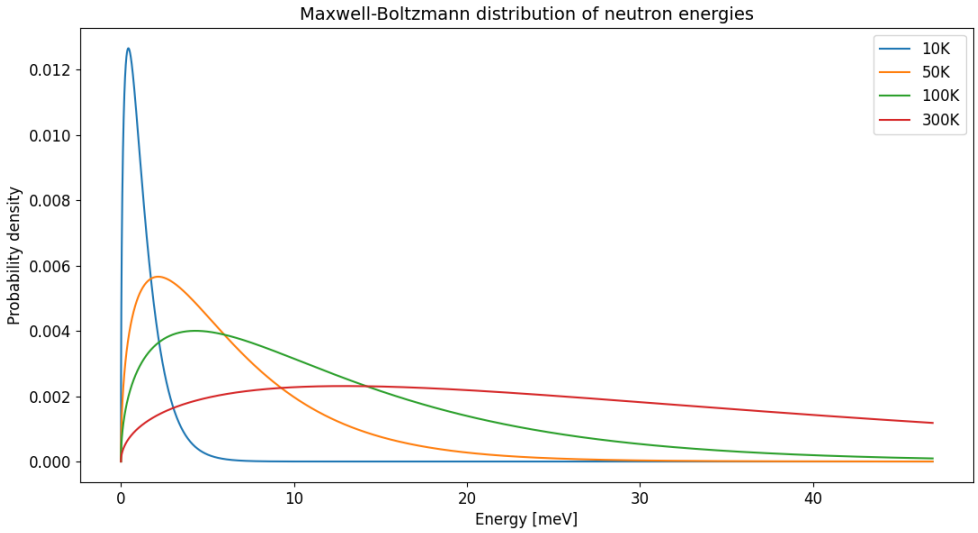

Figure 4: Probability distribution of neutron energies, as they exit a theoretical hydrogen moderator, calculated from a Maxwell-Boltzmann distribution, given as a function of temperature. A Maxwell-Boltzmann distribution given in m/v can be found in Appendix A Figure 26.

description is necessary. According to the equipartition theorem, average kinetic energy $< E >$, can be related to the temperature by the following equation [28]:

$$< E >= \frac{1}{2} m_n < v^2 >= \frac{3}{2} k_B T \tag{8}$$

where m_n is the mass of the neutron and $< v^2 >$ is the average of the neutron squared speed and k_B the Boltzmann constant (≈ 1.38 m^2 kg s^{-2} K^{-1}). The distribution the neutrons take once exiting the moderator will follow a specific type of distribution, namely a Maxwell-Boltzmann distribution.

Figure 4 is a plot of neutron energy distributions at different temperatures according to a Maxwell-Boltzmann probability density function. Vibrational density of states (VDoS) can give a good approximation to what distribution of energies neutrons will have when exiting a potential moderator incorporating these materials. In order to properly understand the data presented herein, some scattering theory is required.

2.3 Neutron Scattering

A scattering event between neutron and a sample can be characterized by an exchange of energy, E, and momentum $\boldsymbol{P}$. This interaction is schematically

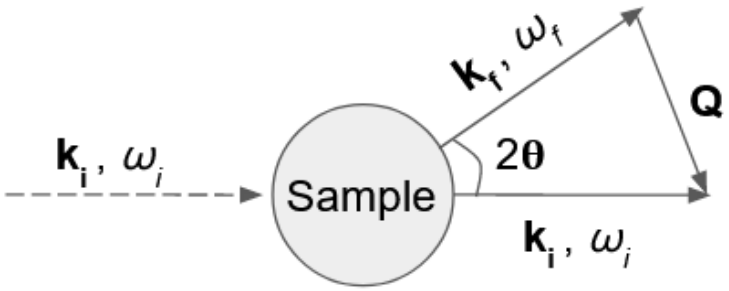

Figure 5: A schematic representation of a neutron being scattered by a sample. Figure altered and redone from reference [3].

depicted in Figure 5. Here an incident neutron, with a wavevector, $\boldsymbol{k_i}$, and angular frequency, ω_i, is scattered off of a sample resulting in the neutron leaving with a final wavevector, $\boldsymbol{k_f}$, and angular frequency, ω_f.

The particle-wave duality of the neutron allows the momentum transfer to be expressed as [29]:

$$\boldsymbol{P} = \hbar\boldsymbol{k_i} - \hbar\boldsymbol{k_f} = \hbar\boldsymbol{Q} \tag{9}$$

where $\hbar$ is Planck's reduced constant $(h/2\pi)$ while:

$$\boldsymbol{Q} = \boldsymbol{k_i} - \boldsymbol{k_f} \tag{10}$$

The energy transfer can be related similarly by:

$$E = \hbar(\omega_i - \omega_f) \tag{11}$$

The energy/momentum gained, or lost, by the scattered neutron is equal to that lost, or gained, by the sample (see Figure 6).

Scattering between the neutron and the sample can usually be split into two categories, Elastic, Figure 6a, and inelastic, Figure 6b, scattering. For elastic scattering there is no exchange in energy, i.e. Eq. 11 is equal to 0. This condition implies that there is no change in the modulus of the wavevector, and by extension the wavelength, λ;

$$|\boldsymbol{k_i}| = |\boldsymbol{k_f}| = \frac{2\pi}{\lambda} \tag{12}$$

remains unchanged after an elastic scattering event takes place. This is useful for diffraction experiments as the elastic scattering of neutrons into different

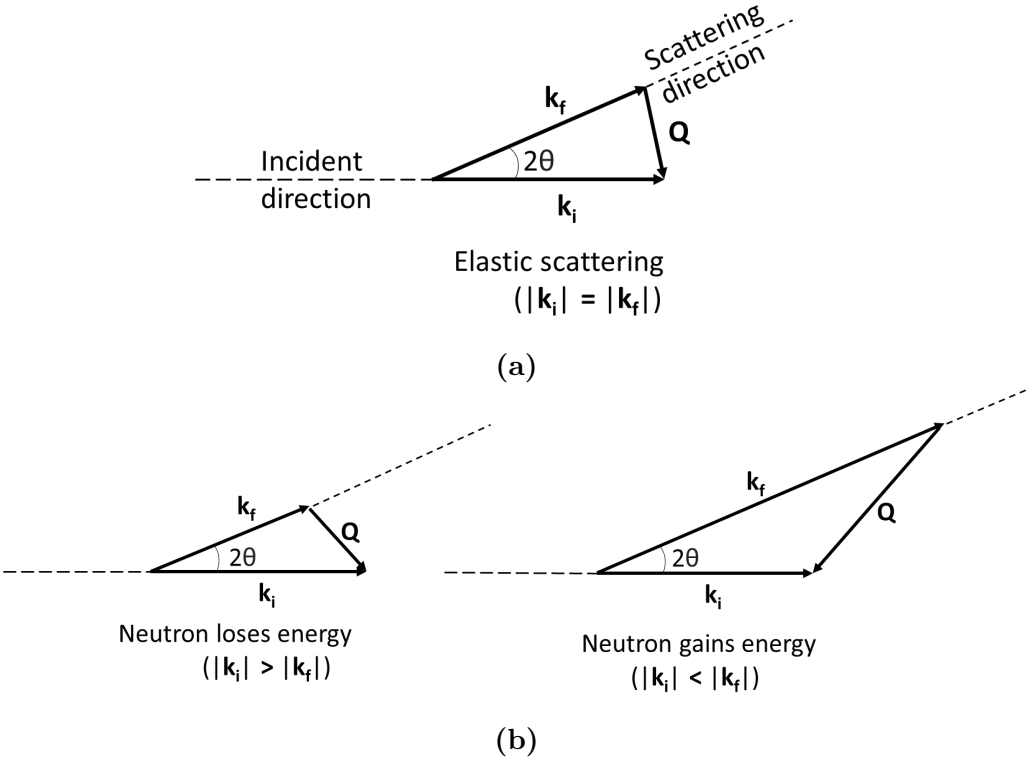

Figure 6: Scattering triangles representing different ways neutron can interact with a nucleus. a) Elastic scattering, where $|\boldsymbol{k_i}| = |\boldsymbol{k_f}|$, and the exchange interaction is strictly through change in vector direction. b) two methods of inelastic scattering interactions, one where the neutron looses energy by transfer to the incident nuclei ($|\boldsymbol{k_i}| > |\boldsymbol{k_f}|$) and one where the neutron gains energy by receiving it from the incident nuclei ($|\boldsymbol{k_i}| < |\boldsymbol{k_f}|$). Figure altered and redone from reference [30].

directions can be used to determine the positions of nuclei in a sample allowing the mapping of its overall structure. If the scattering angle is restricted to range between 1-10°, we talk about small-angle neutron scattering. The principles behind SANS is base on the fact that the intensity of scattered neutrons is proportional to the size and number of scattering particles within a sample. By restricting the scattering angle, it becomes possible to probe more macroscopic structures ranging from 10 to thousands of Angstroms in scale. This allows for the structural study of biomolecules, proteins, polymers as well as colloidal nanoparticles [31].

2.4 Inelastic Neutron Scattering

The 'scattering law', $S(\boldsymbol{Q},\omega)$, is a four dimensional quantity that incorporates all the information measured from a scattering experiment. The momentum transfer, $\mathbf{Q}$, which is a 3-dimensional vector, and the energy transfer, $\omega = \omega_i - \omega_f$, make up the four dimensions of the scattering law. The scattering law is often separated into three parts; elastic, quasi-elastic and inelastic. Thus, the full scattering law can be expressed as the sum of each contribution [32]:

$$S(\boldsymbol{Q},\omega) = S_E(\boldsymbol{Q},\omega = 0) + S_{QE}(\boldsymbol{Q},\omega) + S_{IN}(\boldsymbol{Q},\omega) \tag{13}$$

Here E denotes elastic, QE, quasi-elastic (QENS) and IN, inelastic (INS). Quasi-elastic neutron scattering (QENS) is the motion related to energy exchange close to 0, i.e. the broadened band left and right of the elastic line expressed in Figure 7. This energy transfer range gives information on diffusive motion, rotation and the disorder of a system. Since this region is much lower in energy than that of phonons and molecular vibrations, colder neutrons are necessary in order to accurately probe it, in particular if higher resolution is required.

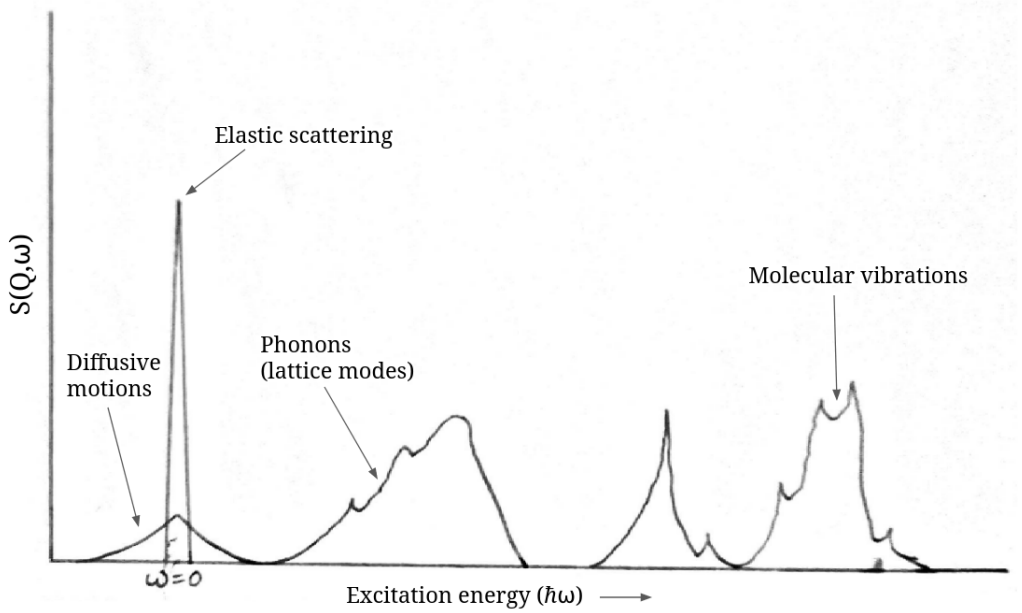

Figure 7: Hypothetical INS spectrum of a molecular crystal illustrating in schematic form different kinds of possible excitations across a wide frequency range. Redone from reference [3].

Inelastic neutron scattering is related to the vibrational modes of a sample. Typically, for a solid state system, we would have a crystal lattice. In this crystal lattice there are two types of modes, acoustic and optical modes [33]. These modes are often referred to as phonons, a quasi-type particle, and refer to the types of vibrations that can occur in an ensemble [34]. In a crystal lattice acoustic modes are either longitudinal (y- and x-axis motion) or transverse (z- and x-axis motion) waves that involve the motion of atoms inside this crystal lattice, in the same direction as the propagating wave. In our case, propagating neutrons. These modes are termed acoustic as they do not change the polarization of light (the criteria for optical modes) and are generally lower in energy (frequency) and velocity. Optical modes on the other hand involve the motions in a crystal lattice that change the polarization of light passing through. These vibrations are typically higher in frequency and velocity than the aforementioned acoustic modes. Like acoustic modes, two types of optical modes exist: longitudinal optical (LO) and transverse optical (TO). In LO modes, all atoms in the lattice move in phase with each other while in TO modes, some atoms move in the same direction of the propagating wave while others move perpendicular to it, resulting in a change of lights polarization [33]. These vibrations also occur in amorphous solids, but due to their randomly arranged atoms they lack any long range order. As a result, the phonon spectrum of an amorphous solid is broad and continuous, without any well-defined dispersion relations. This phonon dispersion relation describes the the interatomic forces at play within a crystal and are well defined for crystal solids. The phonons in amorphous solids are associated with localized atomic vibrations and leads to phonon bandgaps which are characteristic of crystalline solids. An important difference between phonons in crystalline and amorphous solids is their scattering behaviour. In crystalline solids, phonons can scatter off defects, impurities and boundaries, which can affect their propagation and leads to phonon localization. In amorphous solids, phonon scattering is dominated by anharmonic effects, such as phonon-phonon scattering, which can lead to thermal conductivity reduction and phonon damping [35]. These modes are illustrated as the lattice modes depicted in Figure 7. For higher excitation energies we arrive at the energy scale of molecular vibrations [6].

2.5 Vibrational INS Spectroscopy

Vibrational INS spectroscopy refers to spectra of a material gathered by analyzing the change in neutron energy as they pass through the sample under study. These inelastic scattering events are the fundamental process in neutron thermalization [36] and thus INS spectroscopy is an ideal experimental

technique for analyzing moderating materials. IR spectroscopy is reliant on changes in dipole moments and Raman is reliant on Raman active modes (i.e. change in polarizability) in order to generate spectra and as such both techniques need to be employed in order to investigate all 3N-6 available vibrational modes (for non-linear molecules) of a sample. This is not the case for vibrational INS spectroscopy. Neutrons interact primarily with the nucleus of an atom which renders this technique exempt from selection rules and all vibrational modes are essentially measurable. Furthermore, neutron scattering is sensitive to light elements and especially hydrogen which is difficult to detect using other spectroscopic techniques.

INS spectroscopy can be either coherent, incoherent or both. Coherent INS spectroscopy gives information regarding the collective motions of a solid state system whereas the incoherent counterpart involves the correlations between the position of the same nucleus at different times and as such gives information on the motions of single particles. Whether the scattering is primarily coherent or incoherent is dependant on the coherent and incoherent scattering cross-section's of the scattering nuclei [37], [38]. Mathematically the coherent and incoherent counterparts of the scattering function (Eq. 13) starts with the van Hove function [38]:

$$G(\boldsymbol{r},t) = \frac{1}{N}\int \sum_i \sum_j \delta[\boldsymbol{r'} + \boldsymbol{r} - \boldsymbol{r_j}(t)]\delta[\boldsymbol{r'} - \boldsymbol{r_i}(0)]d\boldsymbol{r'} \tag{14}$$

where $G(\boldsymbol{r},t)$ is simply the time-dependant generalization of the pair distribution function, g(r), of a system of interaction particles. $G(\boldsymbol{r},t)$ is a dynamical correlation function in real space, that describes the spatial as well as the temporal distribution of particle-pairs. It is the probability of finding a particle at position $\boldsymbol{r}$ at a specific time t given that one of the two particles of the pair was located at the point of origin at $t = 0$. Taking the spatial Fourier transform of $G(\boldsymbol{r},t)$ results in the intermediate scattering function:

$$I(\boldsymbol{Q},t) = \int_{-\infty}^{\infty} G(\boldsymbol{r},t)exp(-i\boldsymbol{q}\cdot\boldsymbol{r})d\boldsymbol{r} \tag{15}$$

The neutron scattering length, b, varies from nucleus to nucleus due to the neutron-nucleus spin orientations being random. Therefore, the scattering length for any specific collision pair, will have an average value as well as fluctuations from the average. This is where terms such as coherent and incoherent scattering comes into play, as coherent scattering is from the interference terms whereas incoherent scattering arises from fluctuations between independent sites. Thus, incoherent scattering reveals the motion of atoms

and coherent scattering detects pair correlations. This allows for the spatial Fourier transform of the time-dependent pair distribution function, $I(\boldsymbol{Q}, t)$, to be separated into coherent and incoherent counterparts:

$$I_{inc}(\boldsymbol{Q}, t) = \sum_i b_{inc}^2 < exp[-i\boldsymbol{Q} \cdot \boldsymbol{r}_i(0)] exp[i\boldsymbol{Q} \cdot \boldsymbol{r}_i(t)] > \tag{16}$$

$$I_{coh}(\boldsymbol{Q}, t) = \sum_{i,j} b_{i,coh} b_{j,coh} < exp[-i\boldsymbol{Q} \cdot \boldsymbol{r}_i(0)] exp[i\boldsymbol{Q} \cdot \boldsymbol{r}_i(t)] > \tag{17}$$

The incoherent neutron scattering length, b_{inc}^2 of ^{1}H is a magnitude larger than that of most other elements [25]. This means that ^{1}H dominates the incoherent counterpart of a scattering experiment. This experimentally measured quantity is of course the scattering law, $S(\boldsymbol{Q}, \omega)$, which is the time Fourier transform of $I(\boldsymbol{Q}, t)$ and is similarly to $I(\boldsymbol{Q}, t)$, also split into a coherent and incoherent counterpart.

$$S_{inc}(\boldsymbol{Q}, \omega) = \int_\infty^\infty I_{inc}(\boldsymbol{Q}, t) e^{-i\omega t} dt \tag{18}$$

$$S_{coh}(\boldsymbol{Q}, \omega) = \int_\infty^\infty I_{coh}(\boldsymbol{Q}, t) e^{-i\omega t} dt \tag{19}$$

In essence, $S(\boldsymbol{Q}, \omega)$ represents the frequency-dependent distribution of dynamic modes, weighted by their respective amplitudes. Equations 18 and 19 demonstrate that by tracking the atomic positions over time through molecular dynamics (MD) simulations all neutron scattering properties can be computed with ease. It is also possible to calculate theoretical INS spectra with the help of AbINS a new generation of software, where theoretical $S(\boldsymbol{Q}, \omega)$ are calculated using DFT calculations [39]. When probing the vibrational modes of a molecular system through spectroscopy, and especially INS spectroscopy, the temperature of the sample, when measuring, becomes vital. At 0 K, a classical system experiences solely elastic scattering since there is no motion. When the system receives thermal energy, its vibrations become active, resulting in a decrease of elastic incoherent scattering, which is proportional to $exp(- < u^2 > \boldsymbol{Q}^2)$, where $< u^2 >$ represents the average H-weighted atomic mean-square displacement (MSD) which is temperature dependent. Therefore, in order to minimize the thermal broadening of the spectra, low temperatures are necessary for conducting INS studies on materials.

2.6 Density Functional Theory

Quantum mechanical calculations revolve around finding solutions that satisfy the Schrodinger equation. More specifically the time independent Schrodinger equation:

$$\hat{H}\Psi_n = E_n\Psi_n \tag{20}$$

The wavefunction Ψ gives a lot of information about molecular systems. The system's potential energies, the most stable geometries as well as the vibrational electronic energy levels. $\hat{H}$ is the Hamiltonian operator. The Hamiltonian is a differential operator which represents the total energy of the system;, i.e. the potential and kinetic energies. Ψ_n is a set of eigen functions with associated eigenvalues E_n, that satisfy the Hamiltonian. Each of the solutions are referred to as eigen states. The detailed definition of the Hamiltonian depends on the system being described. Some well known examples of this includes the particle in a box and the simple harmonic oscillator. In these examples the Hamiltonian adopts a simple form and in this simplified form the equation can be solved exactly. However, this is not the case for more complex systems, such as molecules and surfaces. Since these systems have many interacting parts that scale in complexity with the number of electrons and nuclei in the system. In such a system, consisting of M nuclei and N electrons in the absence of an external magnetic or electric field, the Hamiltonian may take the form:

$$\hat{H} = -\frac{1}{2}\sum_{i=1}^{N}\nabla_i^2 - \frac{1}{2}\sum_{A=1}^{M}\frac{1}{M_A}\nabla_A^2 - \sum_{i=1}^{N}\sum_{A=1}^{M}\frac{Z_A}{r_{iA}} + \sum_{i=1}^{N}\sum_{j>1}^{N}\frac{1}{r_{ij}} + \sum_{A=1}^{M}\sum_{B>A}^{M}\frac{Z_A Z_B}{R_{AB}} \tag{21}$$

The first two terms are the kinetic energy of the i'th and A'th electron and nucleus, respectively. The next term is the electrostatic attraction between electrons and nuclei and finally the last two are the electrostatic repulsion between the electrons and nuclei, respectively. This is where the complexity reveals itself as one needs to consider all possible interactions between electrons and nuclei simultaneously. One approximation that helps reduce the equations complexity, the Born-Oppenheimer approximation, makes use of the observation that electrons and nuclei differ in mass by 3 orders of magnitude.

Using this observation, the terms involving nuclei kinetics and nuclei-nuclei repulsion can be dropped from the Hamiltonian, simplifying it into an electronic and a nuclear part. Resulting in what is called the molecular Hamiltonian [40]:

$$\hat{H} = -\frac{1}{2}\sum_{i=1}^{N}\nabla_i^2 - \sum_{i=1}^{N}\sum_{A=1}^{M}\frac{Z_A}{r_{iA}} + \sum_{i=1}^{N}\sum_{j>1}^{N}\frac{1}{r_{ij}} = \hat{T} + \hat{V}_{NE} + \hat{V}_{ee} \tag{22}$$

Where T is the kinetic energy, V_{NE} the electrostatic attraction between electron and nuclei and V_{ee} the electron electron electrostatic repulsion. Most systems can be approximately described entirely by this electronic Hamiltonian. However, even with the applied approximations, solving Schrodinger's equation is no trivial matter as the part of the electronic Hamiltonian that describes electrostatic repulsion between electrons still remains a many body problem as each electron experiences the electrostatic repulsion of each other electron simultaneously. To get past this problem an approximation needs to be made. The solution is density functional theory (DFT) [41], [42]. By expressing the electrostatic repulsion potential as a function of density we can vastly reduce the computing power necessary for calculations. Instead of considering 3N interactions, with N being the number of electrons, we can express this electrostatic repulsion by just 3 parameters, x, y and z.

Through a long history of developing and experimental verification density functional theory has settled on a mixture of local density approximations (LDA), generalized gradient approximations (GGA) as well as meta-GGA approximations [41]. All these mathematical approximations for exchange-correlation functionals, mixed with some experimental optimization of fractional contributions for each of these, has resulted in the B3LYP functional:

$$E_{xc}^{B3LYP} = 0.2E_x^{HF} + 0.8E_x^{LDA} + 0.72\nabla E_x^{B88} + 0.81E_c^{LYP} + 0.19E_c^{VWN} \tag{23}$$

Which is up to now the most commonly used, as well as most precise, functional utilized in computation chemistry[41]–[44]. For more in depth background on DFT-theory and how to apply basis sets to calculations, please refer to Appendix A. To validate the accuracy of the single molecule DFT calculations, theoretical Raman and IR spectra were generated based on them and then compared to experimental spectra.

2.7 Raman & IR Spectroscopy

Both Raman and IR spectroscopy make use of electromagnetic radiation's interaction with matter to probe the physical properties of a sample [45]–[47]. Figure 8 demonstrates various ways that electromagnetic radiation can interact with a sample.

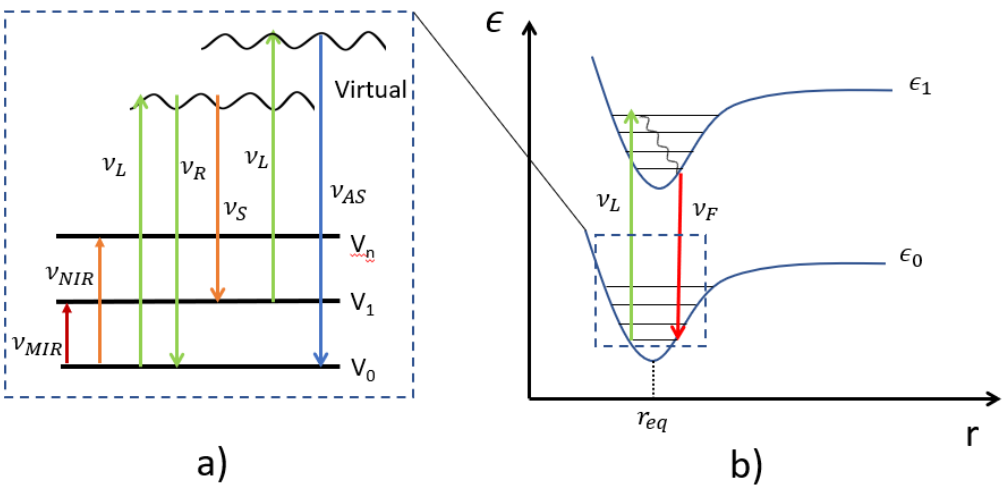

Figure 8: Jablonski diagram detailing various interactions between electromagnetic radiation and matter. a) Left to right, ν_{MIR}; mid infrared (400 to $4000cm^{-1}$); ν_{NIR}, near infrared (4000 to $1400cm^{-1}$); ν_L, incident laser; ν_R, Rayleigh scattering (elastic scattering); ν_S, Stokes and ν_{AS}, anti-Stokes. $V_{0..n}$ indicate the vibrational modes in between the ground, ϵ_0, and excited, ϵ_1, states of b). b) Left to right, ν_L, incident laser and ν_F, fluorescent emission.

In Figure 8a), starting from the left of the diagram, we see two regimes of infrared (IR) absorption, mid infrared (MIR) and near infrared (NIR). These two regimes refer to the energy scale of the electromagnetic radiation used to probe with, with NIR being higher in energy (shorter in wavelength) than MIR. In the diagram, also called a Jablonski diagram, we observe various steps on a ladder. These steps refer to the vibrational levels associated with a particular molecular vibrational mode. Since NIR and MIR light operate on the same energy scale as molecular vibrations, we can use it to measure a samples absorption. This information can then be used to verify the contents of a sample in order to infer the structure of its constituents. However, infrared spectroscopy is reliant on the change in dipole moment as a function of molecular vibration in order to produce a signal and therefore some modes will not be visible in the spectra. This is where Raman spectroscopy comes into play. While IR spectroscopic analysis relies on the absorption properties between radiation and matter, Raman makes use of powerful mono-chromatically filtered laser sources in order to excite short lived "virtual" states, predominantly releasing elastically scattered photons, so called Rayleigh scattering [47].

Returning to Figure 8a) we observe five more regimes after NIR. Again, going from left to right, we observe, first off, that the incident laser, ν_L, excites

a vibrational mode going from the ground state into a virtual state. The next regime depicts Rayleigh scattering (ν_R), where we go from the now excited, virtual, state back to the ground state. Thus, resulting in a signal indicating no energy exchange (elastic scattering). When doing Raman spectroscopy we measure the stokes shift of light. Stokes shift occurs when the virtual state relaxes back to a vibrational mode higher in energy than the one it was excited from, releasing a photon lower in energy than that of the incident photon.

Then, finally, we have another example of an incident photon, ν_L, though this time it excites the molecular vibration from an already excited state. In the example given, this then results in the previously excited state, now virtual state, returning all the way down to the ground state, releasing a photon higher in energy than that of the incident photon. This is what we call an anti-Stokes shift, ν_{AS} [47]. Furthermore, the unintentional possibility of causing an excitation beyond the virtual states exists, causing electronic transitions that result in unwanted fluorescent emissions (Figure 8b)).

3 Methods

3.1 Experimental Details

3.1.1 Inelastic Neutron Scattering Spectroscopy

Both thymol and p-cymene's inelastic neutron scattering (INS) spectra were recorded by the TOSCA neutron spectrometer at ISIS Neutron and Muon Source at the Rutherford Appleton Laboratory, United Kingdom [4].

TOSCA is a time of flight (TOF), indirect-geometry inelastic neutron spectrometer (see figure 9) [48], [49]. Here neutrons that scatter from a sample are detected at a fixed energy range between 4.1 and 3.5 meV. This is accomplished by Bragg reflecting incoming neutrons using a pyrolytic graphite analyzer with a 2 mm thickness and a mosaic spread of 2.5° [50], [51]. The pyrolytic graphite is oriented in such a way as to make use of the (002) Bragg reflecting plane. This translates to a 0.3354 nm distance between the planes. The energy of the incident neutron is then calculated using a well know relation [52]:

$$t = \frac{L_0}{\nu_0} + \frac{L_1}{\nu_1} \tag{24}$$

where L_0, L_1, ν_0 and ν_1 are the incident (index 0) and scattered (index 1) flight-path lengths and neutron velocities, respectively. Typical values for

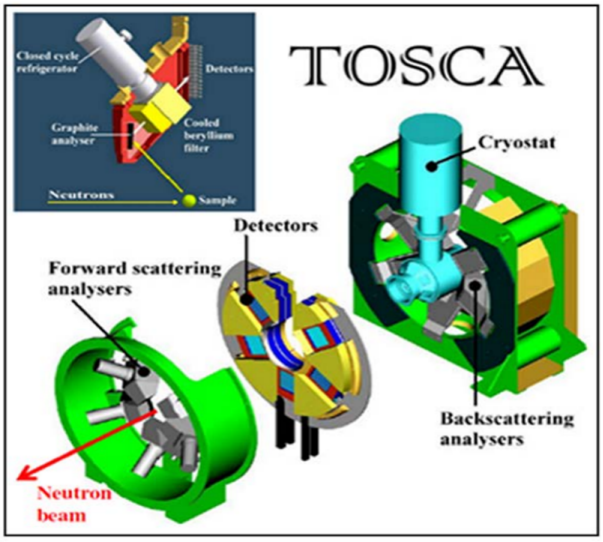

Figure 9: Schematic diagram of the TOSCA neutron spectrometer at ISIS [48].

the neutron flight-paths at TOSCA are: $L_0 = 17.00$ m, $L_1 = 0.55 - 0.70$ m. The high-order harmonic frequencies from the graphite analyzers are reduced by a beryllium-cadmium filter kept a cryogenic temperatures and acts as a high-pass filter for the wavelengths. As one could imagine, the uncertainty in L_1 dominate the energy resolution of the instrument. This translates to a proportional increase in uncertainty of the momentum transfer, $\mathbf{Q}$, with increase in frequency, ω. However, for the purpose of probing vibrational density of states (VDos) and phonon density of states, the $\mathbf{Q}$-dependence is generally not crucial. TOSCA houses both forward and backward detectors which allows the detection of low value energy transfers by exploring two closely related but slightly different ($\mathbf{Q}$, ω) trajectories, and high energy transfers by either the forward or backward detector banks [48]. The INS resolution of TOSCA is $\approx 1.25\% \cdot E_t$, where E_t denotes energy transfer [50]. Figure 27 in Appendix A shows a plot of TOSCA's resolution as a function of energy transfer for the current, and previous, generations of the instrument.

Enough sample material to fill the sample holder (ideally more than 1 gram) was compacted into an aluminium sachet and placed into the 4 x 4.8

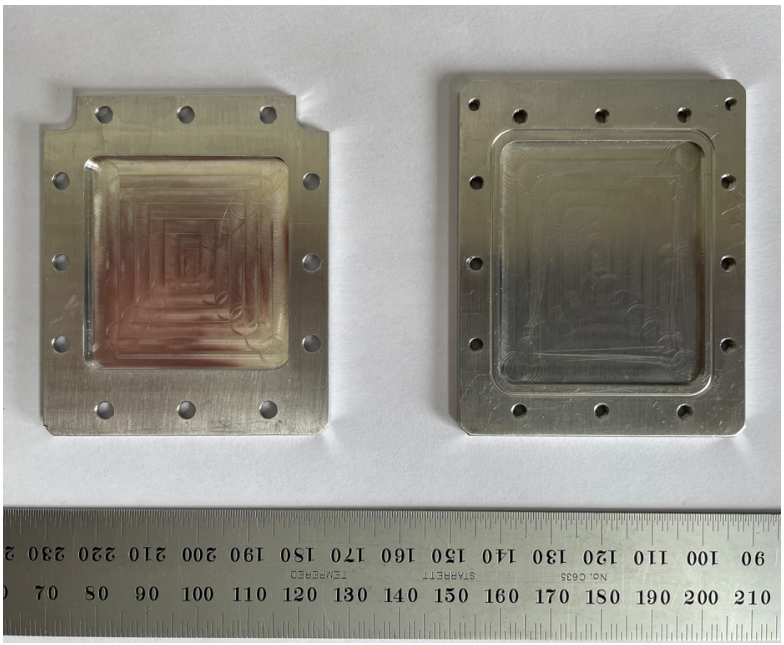

Figure 10: Standard sample holder for the TOSCA spectrometer. Dimensions of the indent are approximately 4 x 4.8 cm^2. Sample is filled into an aluminium sachet and placed into the holder on the right. Indium wire is applied to the grooves of the the sample holder in order to provide an inert, air-tight, seal.

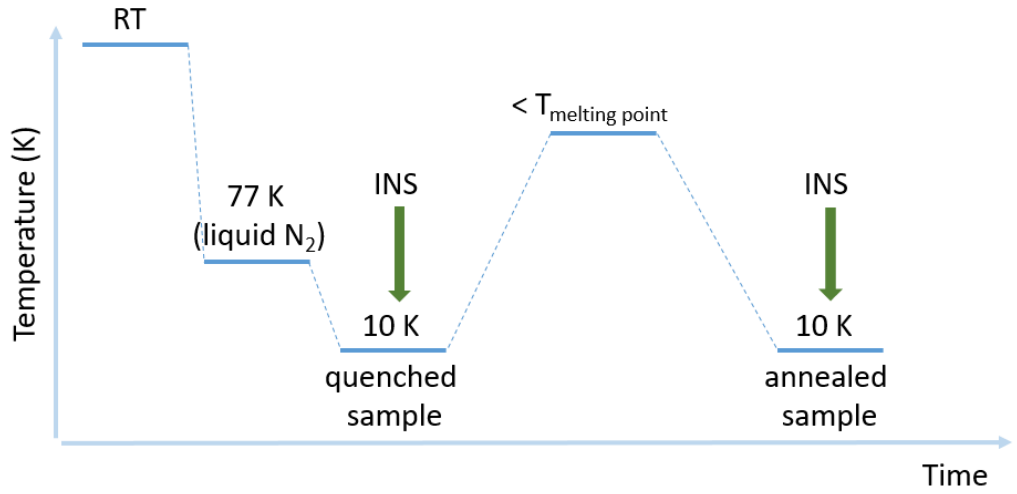

Figure 11: A figure representing the process of gathering the INS spectra of p-cymene's amorphous and crystal phase, as a function of temperature and temperature. RT is short for room temperature.

cm^2 indent of TOSCA's sample holder and the grooves sealed with indium wire (see Figure 10).

Prior to lowering a sample filled sample holder into the spectrometer, it was first cooled with liquid nitrogen. The sample was then quickly transferred into the TOSCA cryostat where it was allowed to cool to $\approx$ 10 K where after the INS spectra were recorded. At extremely low temperatures, the influence of thermal broadening on the temperature dependence of the mean square displacement of atoms becomes negligible.

p-Cymene is a liquid at room temperature. Since rapid cooling of a liquid sample potentially does not allow molecules within the liquid to reorient themselves to the most favourable position thus potentially creating amorphous solid structure, we decided to anneal p-cymene. This annealing procedure involved keeping the sample at just below p-cymene's melting point ($\approx$ 200 K) for 20 to 30 minutes and then slowly bringing it down to cryogenic temperatures ($\approx$ 10 K) prior to gathering the INS spectra. These two cooling processes for gather the two spectra of p-cymene follow the procedure outlined in Figure 11.

3.1.2 Raman Spectroscopy

A small quantity of the sample (roughly 0.2 - 0.3 g) was put into the sample cell of a specialized centre-stick illustrated in Figure 12, which is designed to

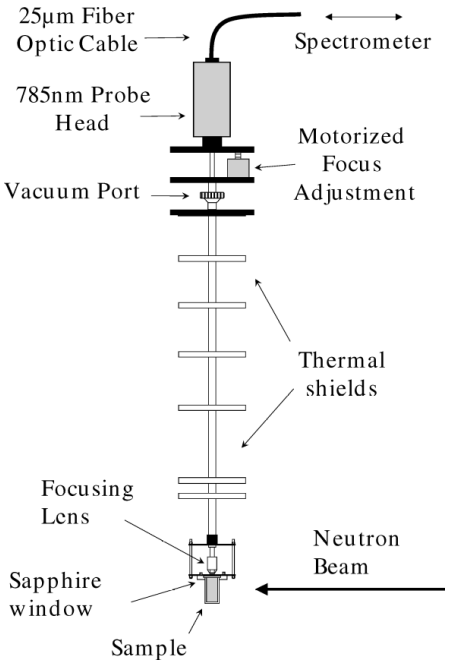

Figure 12: Illustration of the Raman setup with a customized center-stick used in tandem with the Renishaw® inVia Raman spectrometer setup. This specialized stick is designed to also be used for neutron experiments.

also be used for neutron scattering experiments.
The sample is made to cover the entirety of the window to ensure no light scatters off of the aluminium of the cell. The sample cell is then attached to the end of the specialized stick, while the other end is optically coupled to a Renishaw® inVia Raman spectrometer. The stick is then inserted into a 100 mm-bore cryostat which allows for measurements at temperatures between 4 and 350 K. Thymol spectra were recorded on this stick, with the the use of a 785 nm laser at 298 K and at 6 K (temperatures read using a sensor attached directly to the sample cell). The 785 nm laser operated at $\approx$ 200 mW for all measurements carried out on thymol using this setup. This spectrometer had a resolution of 1 to 4 cm^{-1} over a range of 0 to 4000 cm^{-1}.

p-Cymene spectra could not be recorded with the setup described above due to complications attributed to its liquid phase and lack of appropriate seal on the sample holder. This would cause the p-cymene to evaporate when a vacuum was applied to the setup. A Bruker Senterra spectrometer was used for the recording of p-cymene and thymol with a 532 nm laser. Spectra were recorded using 10 accumulations of 10 seconds each with a laser power of $\approx$ 5 mW. The sample is placed on a glass slide and the focus is adjusted manually to ensure that the laser is focused on the sample and the spectra recorded.

All spectra using this setup were recorded at 298 K. The resolution of this instrument was significantly poorer, ranging from 9-18 cm^{-1} over a spectral range of 0 to 4000 cm^{-1} .

3.1.3 IR Spectroscopy

IR spectra were recorded on a Bruker® VERTEX 70v FT-IR spectrometer. The sample material was placed into the instruments sample holder and the spectra recorded. The resolution of this instrument ranges from $\approx$ 0.5-0.7 cm^{-1} over a spectral range of 50 to 6000 cm^{-1}.

3.1.4 Materials

Analytical grade p-cymene and thymol samples were purchased from Sigma-Aldrich Co (St. Louis, Missouri). p-Cymene as a colorless liquid with a purity of $\geq$ 98.5% and thymol as a solid with a purity of 99-101%.

3.2 Computational Details

3.2.1 DFT Calculations & AbINS

Thymol and p-cymene's 3D structure was reconstructed using Jmol [53]. The molecular geometry was obtained from the optimized structure using the GAUSSIAN 16 sotware packages optimization structure algorithm (Berny Optimization Algorithm) [54]. B3LYP level of theory DFT calculations were performed in order to derive both vibrational frequencies and their associated IR-intensities on the optimized structures of both thymol and p-cymene. B3LYP calculations were performed with both 6-31++G(d,p) and 6-311++G(d,p) basis sets. This was accomplished by submitting jobs to SCARF, a high performance computing cluster [55], through batch commands.

Ab initio INS spectra were derived from the vibrational frequencies and associate atomic displacement from equilibrium position matrices (also provided by the GAUSSIAN 16 software output) for each vibrational mode, with the use of AbINS as implimented in the Mantid software package [56]. All plots of INS spectra, both experimental and theoretical, were done using the Mantid software package. All data-files, including Gaussian .log, .com and raw data files from measurements performed on TOSCA, as well as scripts used to plot figures in Mantid, are available at the following repository: https://tinyurl.com/LukasZeppelinMasterThesis.

3.2.2 Ab Initio IR & Raman Spectra

Additional B3LYP/6-311++G(d,p) calculations were performed using the "freq=raman" command in the input file of the Gaussian software in order to extract the Raman active modes as well as the IR-intensities of the vibrational modes. The Gaussian output file from these calculations were opened in ChemCraft's software package [57] which was used to produce theoretical IR and Raman spectra. This software also provided visualization of the motion involved in each vibrational mode and was used to provide the descriptors given in Tables 4 and 5 from the Results Section. For the theoretical Raman as well as IR spectra, a varying degree of Lorentzian broadening was applied (full-width half-maximum) and is expressed in the figure captions. Furthermore, when constructing theoretical Raman spectra for comparison with experimental data the temperature and incident laser's wavenumber, fitting the experimental parameters of the experimental data in question, were input as parameters in ChemCrafts user interface. The Lorentzian broadening applied to the theoretical spectra herein is purely qualitative to improve the aesthetic comparison between theoretical and experimental spectra and is not attributed to the individual instruments resolution, unless stated otherwise.

4 Results

The results in this section include Inelastic Neutron Scattering (INS) spectra as well as IR and Raman spectra that have been gathered for both thymol and p-cymene. B3LYP/6-311++G(d,p) level of theory calculations were performed on single molecules of these two chemicals and theoretical spectra were derived from these. Thus, the following section includes a detailed comparison between experimental and theoretically calculated values as well as verification of the precision of the single molecule DFT calculations.

4.1 Thymol

4.1.1 Experimental INS

Figure 13 shows the INS spectrum of thymol in the energy transfer range between 0 and 500 cm^{-1} gathered at the TOSCA neutron spectrometer at ISIS. In the low energy transfer region from 0 to 200 cm^{-1} (the region of lattice modes) the experimental data presents with a relatively uniform distribution of vibrational density of states (VDoS). Far from perfectly uniform as small peaks are visible throughout the energy transfer range between 20 to 120 cm^{-1}. This slight smoothing of the peaks likely arises from the fact that thymol is of a trigonal $R\bar{3}$ space group containing a mixture of two distinct crystal configurations [58]. Therefore presenting itself with inherently broadened features within this range.

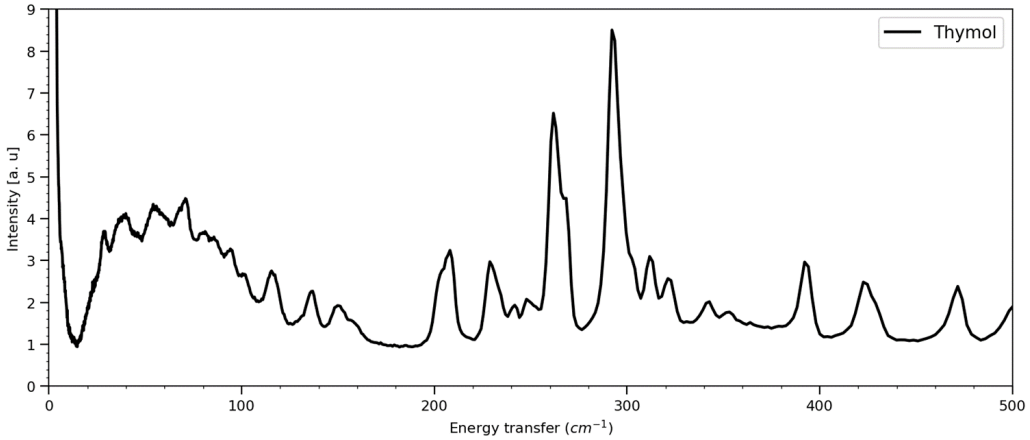

Figure 13: Thymol INS spectrum in the energy transfer range between 0 and 500 cm^{-1} taken at a temperature of $\approx$ 10 K.

4.1.2 INS Experimental & Theoretical Comparison

Figure 14 is the theoretical and experimental comparison between measured and calculated VDoS for thymol. Despite thymol's pseudo-uniform distribution in the low energy range of 0 to 120 cm^{-1}, some of the simulated VDoS seem to overlap perfectly with the experimental data, while others are shifted slightly. Between 20 and 60 cm^{-1} in Figure 14 the calculated INS overlap with each their peak when shifted. The very first peak in the theoretical spectrum is associated with the rotation of the 5-methyl group. The very first peak in the experimental spectrum, which is more easily seen in Figure 13, can be observed as the slight shoulder on which the first theoretical mode overlaps. The next peak in the experimental spectrum $\approx 30cm^{-1}$ is likely also associated with the rotation of the 5-methyl group, although slightly hindered. The next theoretical mode sits between the next two peaks of the experimental spectrum between 40 and 60 cm^{-1}. Both these peaks are associated with the symmetrical rotation of the 2-isopropyl and 5-methyl groups, with the one higher in energy also being attributed to a slightly hindered rotation. The next mode which is barely visible in the theoretical spectrum (between 60 and 80 cm^{-1}) is associated with the bending of the 2-isopropyl and 5-methyl groups. The next mode in the theoretical spectrum, which is also associated with the motion of the 2-isopropyl and 5-methyl group, at $\approx$ 90 cm^{-1}, is hard to assign with any peak of the experimental as it sits in between a number of peaks, likely overshadowed by various acoustic and op-

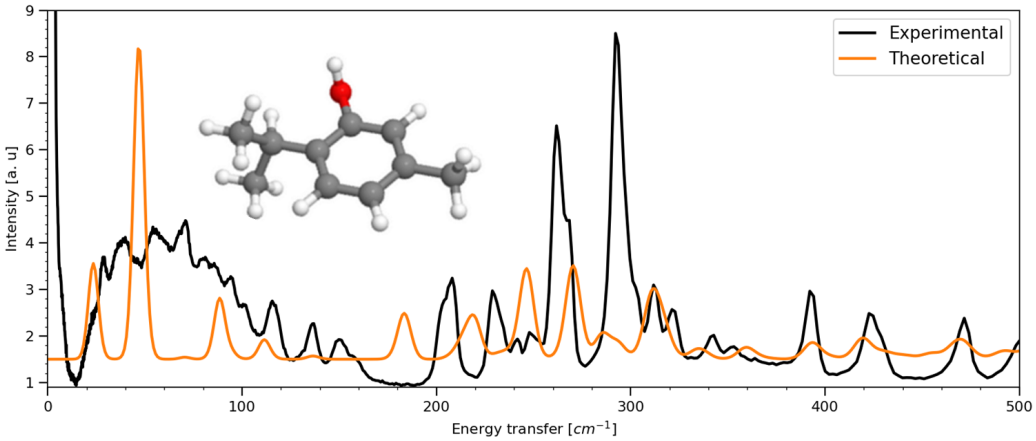

Figure 14: Comparison between experimental (black) and theoretical (orange) INS spectrum of thymol. Theoretical vibrational modes (associated with single molecule optimised geometry) were derived with the help of DFT calculations at the B3LYP/6-311++G(d,p) level of theory.

tical modes. The next two modes in the theoretical spectrum, which are both thought to be related with the motion of the 1-hydroxy and/or 2-isopropyl groups, overlap quite nicely with the experimental INS spectrum. The mode just below 200 cm^{-1} in the theoretical spectrum sits in a valley between two peaks of the experimental spectrum. Among the vibrational modes above 200 cm^{-1}, this particular mode is the only one that deviates slightly. However, the remaining vibrational modes exhibit a remarkable correlation with the experimental values. Notably, above 300 cm^{-1}, almost every theoretical peak aligns perfectly with its corresponding peak in the experimental spectrum. Table 4 attempts to describe the specific vibrational motion assigned to each vibrational mode in the energy range between 0 and 500 cm^{-1}. Figure 15 is an illustration of thymol with some added color grading and benzene carbon numbering to aid in the understanding of Table 4.

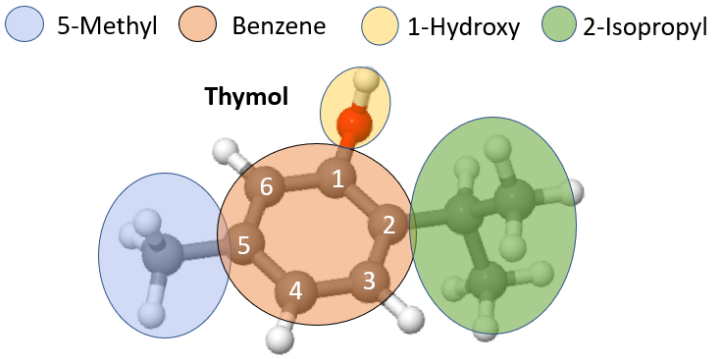

Figure 15: Color coded subsections of the groups associated with thymol's chemical structure as well as benzene carbon numbering to aid the reader in the understanding of Table 4.

Table 4: Thymol: Low energy vibrational modes associated with the optimized structure of thymol calculated at the B3LYP/6-311++G(d,p) level of theory.

Mode No.	Freq (cm^{-1})	Descriptor
1	26	Rotation (twisting) of the 5-methyl group with slight symmetrical stretching of the methyl bonded hydrogens
2	45	Symmetrical rotation of the 2-isopropyl and 5-methyl groups

3	89	Bending of the **2-isopropyl** and **5-methyl** group out of the plane
4	184	Rocking of the **2-isopropyl** group as well as slight rotation of **2-isopropyl's** methyl group furthest from the **1-hydroxy** group
5	216	Wagging of the **1-hydroxy** and **5-methyl** groups with slight counter rotation of **2-isopropyl's** methyl group nearest to **1-hydroxy**
6	220	Wagging of the **1-hydroxy** and **2-isopropyl's** methyl group closest to the **1-hydroxy** group
7	248	Asymmetric rotation of **2-isopropyl's** two methyl groups
8	273	Symmetric rotation of **2-isopropyl's** two methyl groups
9	285	Scissoring of the **1-hydroxy** and **5-methyl** group out of the plane as well as slight rotation of **2-isopropyl's** methyl groups and slight symmetric H-stretching
10	314	Rocking of **2-isopropyl** and **5-methyl** into the plane as well as slight scissoring of **-isopropyl's** methyl groups
11	332	Rotation and slight stretching of **1-hydroxy's** hydrogen
12	394	Hard to describe mode. General vibration and counter motion of all atoms w/ respect to each other
13	419	Scissoring of **2-isopropyl's** two methyl groups out of the plane and general counter vibration of all other atoms
14	471	Hard to describe mode. Mostly characterized by scissoring of **2-isopropyl's** two methyl groups and rocking of **benzene's** carbon's 1 and 6.

Animations for all listed modes can be found in the following repository: https://tinyurl.com/LukasZeppelinMasterThesis.

Many of the low energy modes (<200 cm^{-1}) involve the rotation and/or stretching of methyl and isopropyl groups as well as bending of these in

relation to each other. In a crystal lattice, these motions would be heavily impacted by neighboring molecules due to a number of forces such as van der Waals forces (weak electrostatic interaction) and, most prominently, hydrogen bonding. In addition, as the vibrations are not from a single group, but a mixture, additional vibrational modes of the lattices further broadens the spectrum. For vibrational modes slightly higher in energy (200 to 500 cm^{-1}) we observe that not all peaks in the experimental spectrum are represented in the theoretical. These unassigned peaks are likely due to various acoustic and optical modes that also exist in the crystal lattice as these would not be resolvable through single molecule DFT calculations.

4.1.3 Raman & IR Experimental & Theoretical Comparison

Figure 16 shows a comparison between a theoretically calculated Raman spectrum of thymol from the B3LYP/6-311++G(d,p) level of theory calculations, and one that has been recorded experimentally, at 6 K. In the low energy range between 10 and 150 cm^{-1} there is a low correlation between the spectrum. This is likely due to Raman active lattice modes that are not apparent in the single molecule DFT calculations (i.e. optical modes). Mov-

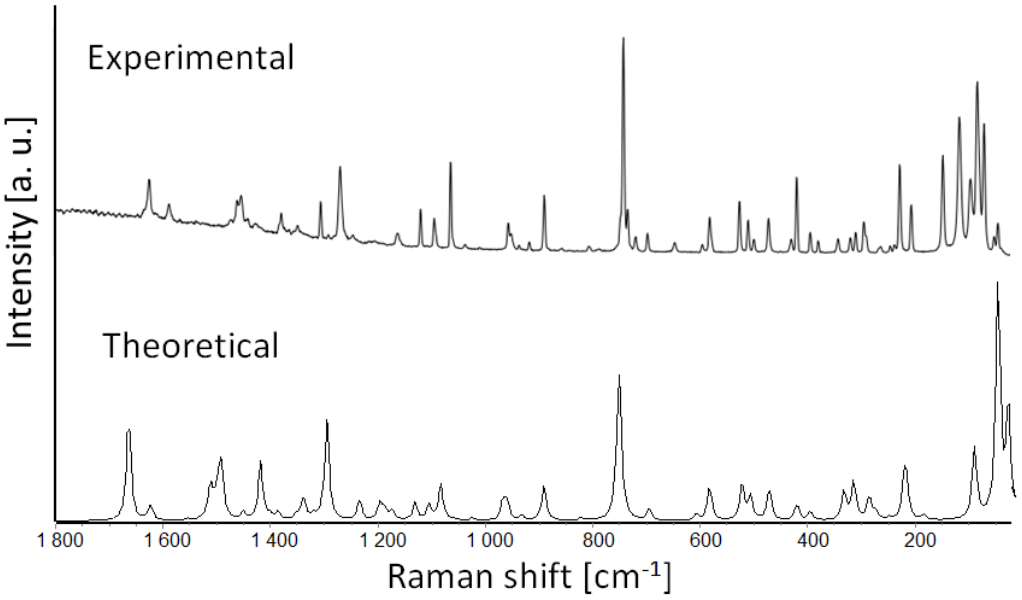

Figure 16: Experimental Raman spectrum of thymol gathered with the use of a 785 nm laser at a temperature of 6 K. Theoretical Raman spectrum of thymol generated with from B3LYP/6-311++G(d,p) level of theory with a temperature parameter of also 6 K with a Lorentzian broadening of 10 cm^{-1}.

ing further up in energy >200 cm^{-1} we start to observe very good agreement between theoretically and experimentally resolved peaks, as the most prominent, and largest peaks, start to overlap with each other nicely. Specifically the 3 largest peaks at $\approx$ 750 cm^{-1}, $\approx$ 1300 cm^{-1} and $\approx$ 1650 cm^{-1} overlap very nicely between the two spectrum. In the experimental spectrum, starting from $\approx$ 1150 cm^{-1} a very broad band starts to form and extends throughout the full spectrum and is not presented here, but can be found in Appendix B (Figure 28). This is likely due to some sort of fluorescence that starts to dominate more in the lower temperatures where a majority of states are available to be excited and is considered to be noise, as this is not visible in the room temperature measurements Appendix B Figure 29).

The full Raman spectrum for thymol in Appendix B (Figure 28) also does not show any of the OH-stretches, and CH-stretches are barely noticeable. This is a known issue related to the specific Raman setup used for these measurements and subsequent IR spectrum was recorded, seen in Figure 17, in order to verify their presence.

In Figure 17 we observe both CH- (<3000 cm^{-1}) and OH-stretches (>3000

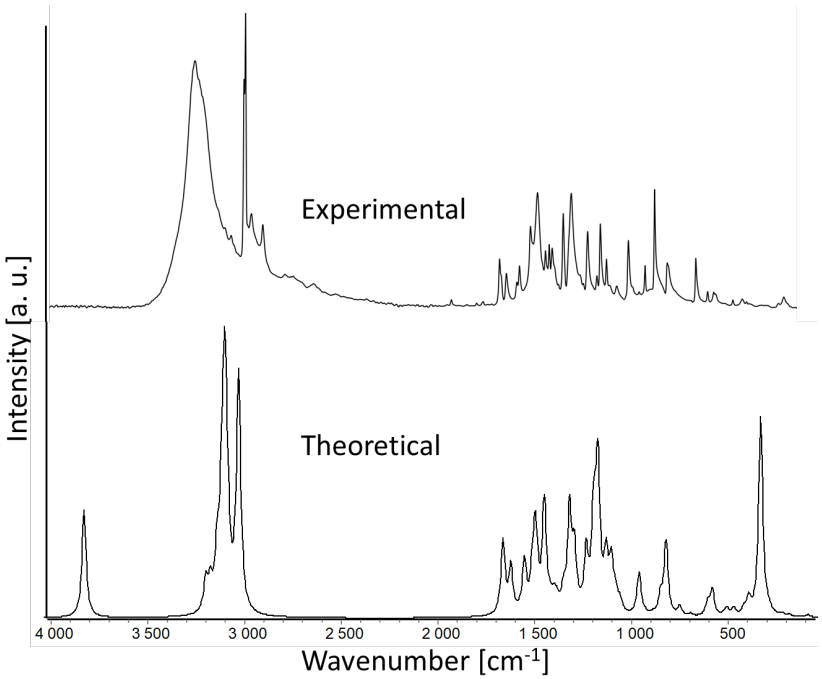

Figure 17: Experimental FT-IR spectrum for thymol compared with theoretical IR spectrum generated from B3LYP/6-311++G(d,p) level of theory with an added Lorentzian broadening of 25 cm^{-1}.

cm^{-1}) in the experimental spectrum. However, the OH-stretches in the theoretical spectrum are shifted higher in energy to $\approx$ 3850 cm^{-1}. This is likely due to the various interactions that are present in a crystal lattice, such as the aforementioned van der Waals forces and hydrogen bonding.

The CH-stretches are in relatively good agreement, although slightly shifted, likely also due to hydrogen bonding between the OH's and CH's. In the lower energy range below <2000 cm^{-1} the overall landscape of the spectrum is also shifted slightly, but are in overall good agreement with each other.

4.2 p-Cymene

4.2.1 Experimental INS

Figure 18 shows two distinctly different INS spectrum of p-cymene both gathered at the TOSCA vibrational INS spectrometer. The key difference between the two spectrum is that when gathering one of the spectrum, p-cymene was allowed to anneal prior to measuring. Since p-cymene is a liquid at room temperature with a melting point (MP = 205 K) well above liquid nitrogen's boiling point (BP = 77 K), the initial procedure of cooling prior to mounting the sample into the spectrometer, was thought to cause the sample to solidify too quickly, resulting in an amorphous structure. This is due to the observation of the particularly uniform distribution of intensity apparent in the energy transfer region between 0 to 200 cm^{-1} in Figure 18.

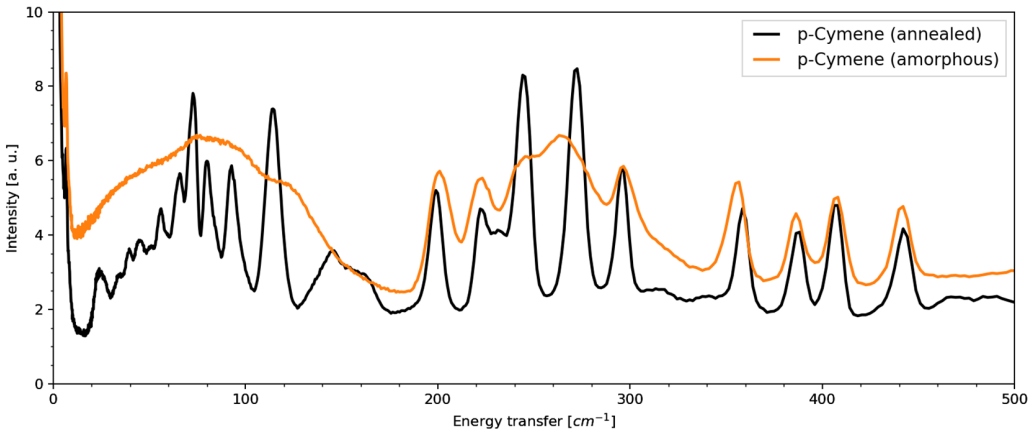

Figure 18: p-Cymene INS spectrum in the energy transfer range between 0 and 500 cm^{-1} taken at a temperature of $\approx$ 10 K. The two spectra of p-cymene were gathered one of an amorphous solid (black) and one where the sample was annealed (orange).

This energy transfer range is in the regime of lattice modes (see Figure 7 from Section 2.4) and the uniform distribution in this range would indicate that the sample does not contain any repeating unit cell. This was then confirmed by a second set of measurements resulting in the annealed version of the sample in Figure 18. This set of measurements differed from the rest in that the sample holder was kept at a steady temperature of $\approx$ 200 K for around 20 to 30 minutes and cooled much slower compared to the quick quenching of the sample in liquid nitrogen. The spectrum gathered after annealing clearly indicates a more ordered structure. Not only are the peaks more distinguishable throughout the whole energy transfer range of the plot, but the energy transfer region between 0 to 200 cm^{-1} shows individual peaks and not just the uniform distribution as the same region exhibited in the amorphous spectrum of p-cymene.

4.2.2 INS Experimental & Theoretical Comparison

In Figure 19 there seems to be an agreement between experimental and theoretically derived VDoS. The very first peak between 20 and 30 cm^{-1}, which is thought to be associated with the rotation of the 4-methyl group, aligns perfectly with the experimental value. The two adjacent peaks in the range of 30 to 60 cm^{-1}, are presumed to arise from rotational motion of the 1-isopropyl group, exhibit complete overlap with their corresponding experimental peaks in the spectrum. The next four peaks of the theoretical

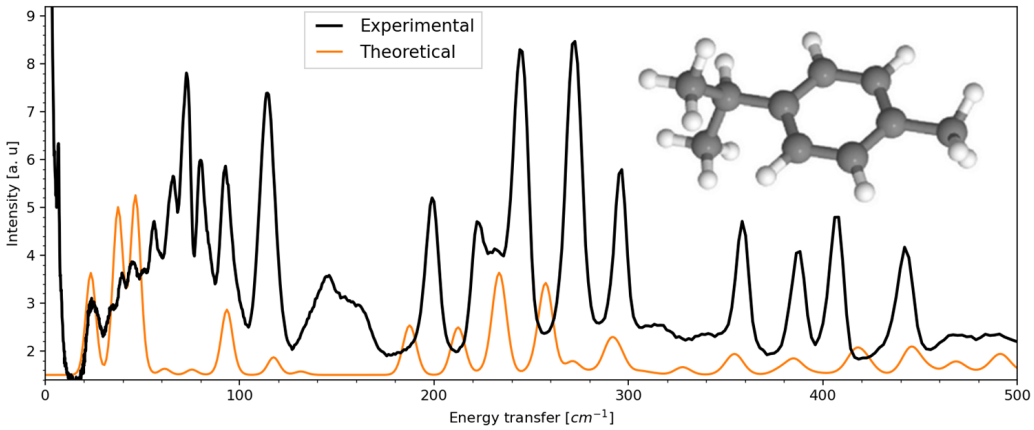

Figure 19: Comparison between experimental (black) and theoretical (orange) INS spectra pf p-cymene. Theoretical vibrational modes (associated with single molecule optimised geometry) were derived with the help of DFT calculations at the B3LYP/6-311++G(d,p) level of theory.

spectrum between 60 and 150 cm^{-1} are mostly attributed to the bending of the 1-isopropyl group and these peaks display a remarkable degree of agreement with their respective peaks observed in the experimental spectrum. In the energy transfer range between 150 and 300 cm^{-1} of the theoretical spectrum there are six peaks which corresponds very nicely with the six peaks that can be seen in the same range of the experimental spectrum. Like with thymol, the theoretical and experimental overlap above 300 cm^{-1} is in very good agreement with each other. The very first peak at $\approx$ 23 cm^{-1} is so well defined in the experimental spectrum that it could indicate ideal behaviour for a cold neutron moderating material.

Table 5 attempts to describe the first couple of vibrational modes for p-Cymene in the low energy range (0 to 500 cm^{-1}). Figure 20 serves to aid the reader in the understanding of Table 5.

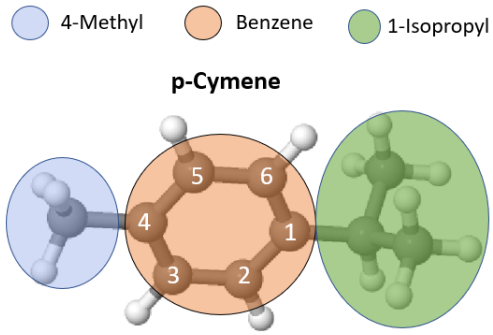

Figure 20: Color coded subsections of the groups associated with p-cymene's chemical structure as well as benzene carbon numbering to aid the reader in the understanding of Table 5.

Table 5: p-Cymene: Low energy vibrational modes associated with the optimized structure of p-cymene calculated at the B3LYP/6-311++G(d,p) level of theory.

Mode No.	Freq (cm^{-1})	Descriptor
1	23	Rotation (twisting) of the **4-methyl** group with slight symmetrical stretching of the methyl bonded hydrogens
2	38	Rotation (twisting) of the **1-isopropyl** group
3	94	Scissoring (bending) of the **1-isopropyl** group with respect to the plane

4	188	Scissoring (bending) of the **1-isopropyl** group out of the plane
5	212	Simultaneous twisting of the **1-isopropyl** methyl groups, and scissoring (bending) of both the **1-isopropyl** group and **4-methyl** group in plane
6	234	Asymmetric rotation of **1-isopropyl's** 2 methyl groups and slight scissoring (bending) of both **1-isopropyl** and **4-methyl** in the plane
7	258	Symmetric rotation of **1-isopropyl's** two methyl groups and slight scissoring (bending) of the **1-isopropyl** and **4-methyl** group out of plane
8	291	Scissoring (bending) of **1-isopropyl's** 2 methyl groups into the plane
9	355	Scissoring of **1-isopropyl's** 2 methyl groups into the plane as well as wagging of the **1-isopropyl** and **4-methyl** group out of the plane
10	386	Twisting of **benzene's** 2, 4, and 6 carbons into the plane and slight scissoring of the **1-isopropyl** and **4-methyl** groups into the plane
11	417	Twisting of **benzene's** 2-5 and 3-6 carbons into the plane
12	445	Slight **benzene** breathing as well as scissoring of **1-isopropyl's** 2 methyl groups into the plane

Animations for all listed modes can be found in the following repository: https://tinyurl.com/LukasZeppelinMasterThesis.

Similar to thymol, a significant portion of the low-energy modes exhibit substantial degrees of unrestricted motion involving the methyl groups, including rotational, stretching, and bending dynamics of both the isopropyl and methyl moieties. However, p-cymene starts to diverge from thymol in the higher energy region (>200 cm^{-1}) when looking into the specific vibrational motions of these modes. The variation can be attributed to p-cymene's lack of a 1-hydroxy group, which leads to a divergence in their respective crystal structures. Most of the modes here are characterized by bending, rocking

and breathing of the benzene ring, and its carbons, whereas for thymol motion of 1-hydroxy group dominate for the vibrational modes up until mode 14 in table 4.

4.2.3 Raman & IR Experimental & Theoretical Comparison

Due to issues with the cryogenic Raman setup, as discussed in the methods section (i.e. imperfect seal on the sample holder), a different type of setup needed to be used in order to record Raman spectra of p-cymene. The spectrum recorded for p-cymene, using the 532 nm FT-Raman setup, is shown in Figure 21. The first thing one notices is the broader peaks in the experimental spectrum of p-cymene as opposed to thymol, using the cryogenic Raman setup. This is due to the low resolution of the instrument ranging from 9 to 18 cm^{-1}, as opposed to the 1 to 4 cm^{-1} for the cryogenic Raman setup. These

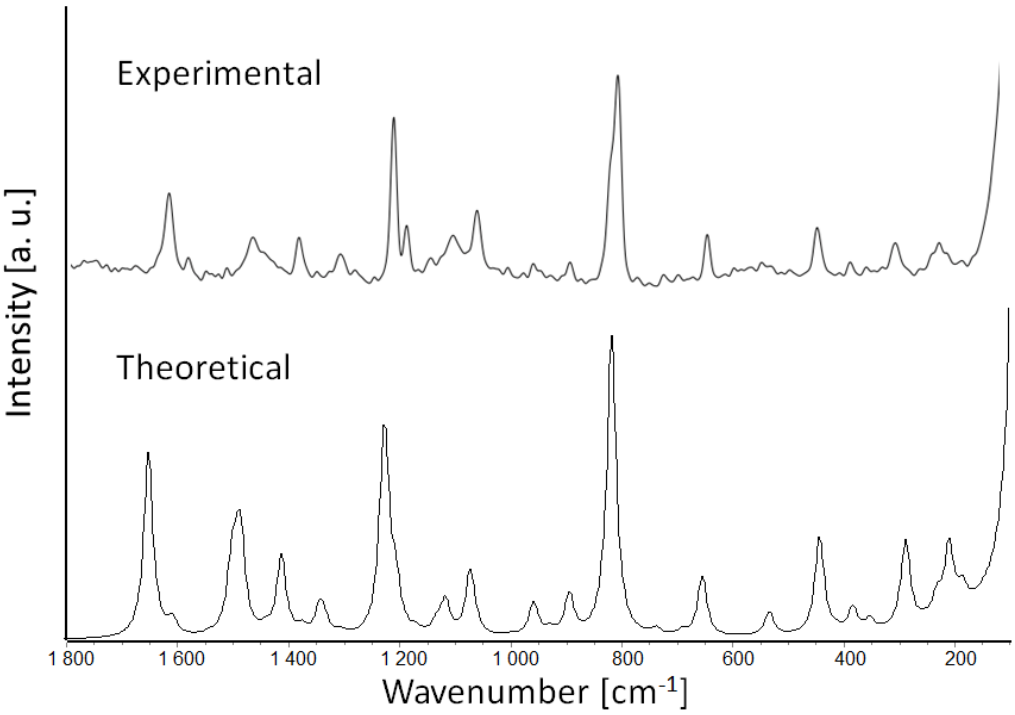

Figure 21: Experimental FT-Raman spectrum of p-cymene gathered with the use of a 532 nm laser at a temperature of 298 K. Theoretical Raman spectrum of p-cymene calculated at the B3LYP/6-311++G(d,p) level of theory with a temperature parameter of 298 K with a Lorentzian broadening of 20 cm^{-1}. The Lorentzian broadening here reflects the resolution of the instrument ranging from 9-18 cm^{-1}.

broadened features are also expressed in the theoretical spectrum through the larger Lorentzian broadening applied in the calculations.

The experimental and theoretical spectrum are generally in quite good agreement with each other, with a majority of the most prominent peaks aligning quite well. The three most prominent peaks at $\approx$ 820 cm^{-1}, $\approx$ 1220 cm^{-1} and $\approx$ 1650 cm^{-1} are, like with thymol, in good agreement with each other. Albeit, with the theoretically calculated peak highest in energy shifted slightly higher when compared with the same peak in the experimental spectrum.

This Raman setup was, as apposed to the cryogenic setup, able to capture the CH-stretches. This can be seen in the full spectrum in Appendix B Figure 32. However, for good measure the IR spectrum of p-cymene was also recorded and can be seen in Figure 22. Here the spectrum are in good agreement, but with the CH-stretches at >3000 cm^{-1} being shifted higher in frequency when compared to the experimental spectrum.

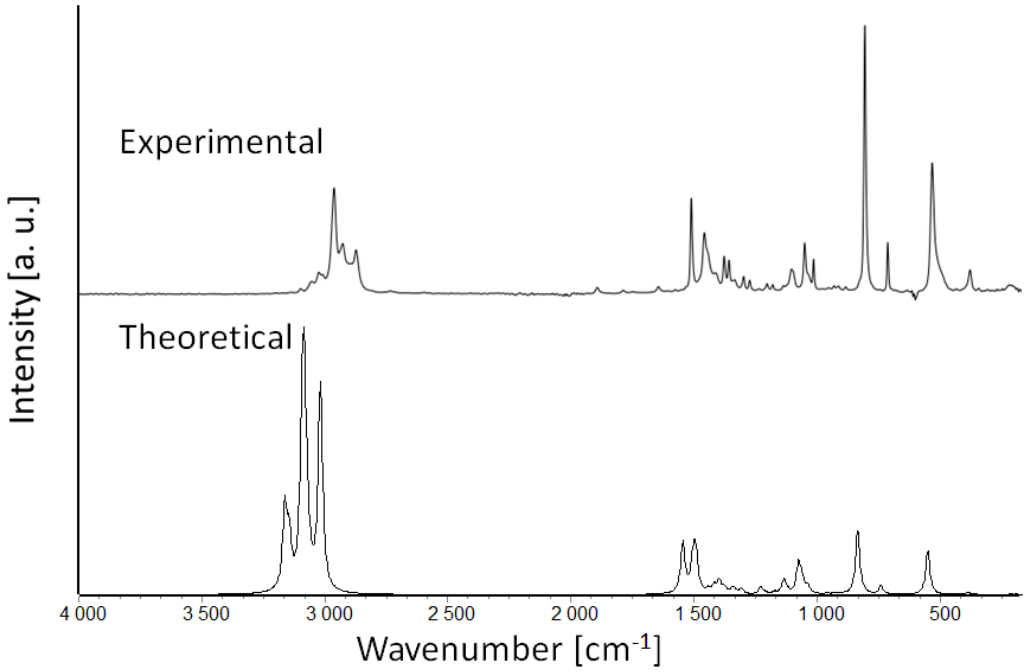

Figure 22: Experimental FT-IR spectrum for p-cymene compared with theoretical IR spectrum generated from B3LYP/6-311++G(d,p) level of theory with an added Lorentzian broadening of 20 cm^{-1}.

5 Discussion

To further understand the results presented in this thesis, a comparison between the theoretical spectra generated from the DFT calculations performed in this work and experimental results collected from literature, is presented.

In Figure 23 an extract from Rajkumar et al's experimental [59], and theoretical spectrum IR spectra, calculated for the single molecule at the B3LYP/6-31+G(d,p) level of theory, are plotted against my own theoretical IR spectrum calculated at the B3LYP/6-311++G(d,p) level of theory for the single molecule. In Figure 23 we can observed that, visually, the theoretical IR spectrum of the B3LYP/6-311++G(d,p) calculation overlap much better with their experimental values than their own theoretical calculations (likely due to their smaller basis set). However, in the high energy range where the OH-stretching takes place both theoretical spectrum are off by 150 to 200 cm^{-1} which is likely due to that calculations refer to the single molecule while

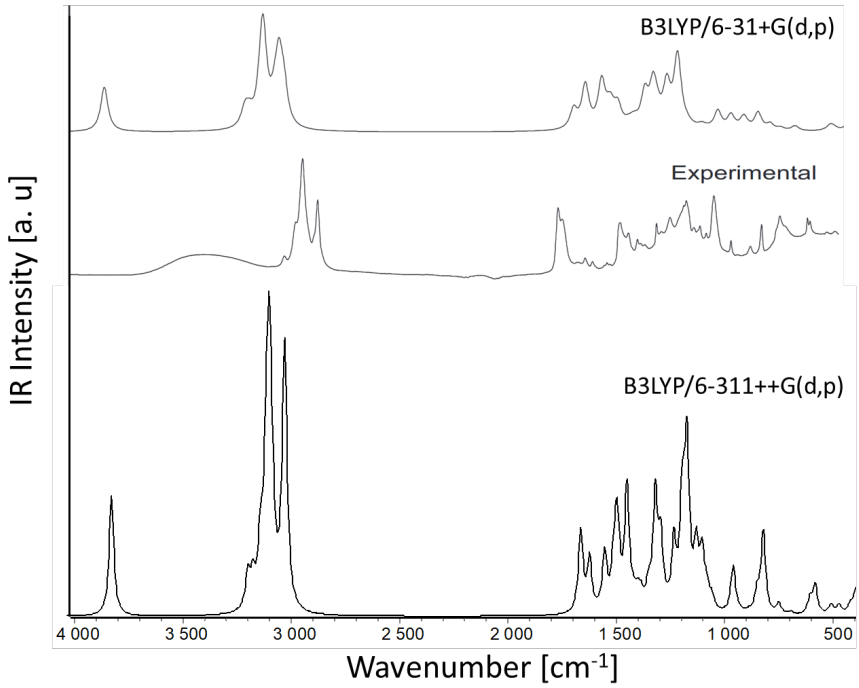

Figure 23: Top: Theoretical IR spectrum of thymol calculated at the B3LYP/6-31+G(d,p) level of theory for the single molecule. Middle: experimental IR spectrum of thymol. Both taken from Rajkumar et al [59]. Bottom: Theoretical spectrum generated from my DFT calculations done at the B3LYP/6-311++G(d,p) level of theory for the single molecule.

experimental data correspond to the solid structure where 1-hydroxyl group engages in hydrogen bonding thus shifting its vibrational frequency towards lower values.

Another study carried out by Schulz et al aimed to characterize the FT-Raman spectrum of common oils from the lamiaceae plant species [60] which included, among others, p-cymene and thymol.

Figures 24 and 25 are comparisons between experimental FT-Raman spectrum, produced by Schulz et al [60], and theoretical Raman spectrum generated from my B3LYP/6-311++G(d,p) DFT calculations. Visually, the theoretically generated Raman spectrum emulate the experimental spectrum extremely well. Figure 24's three most intense peaks characterized by Schulz et al overlap almost perfectly with the three most intense peaks in the theoretically resolved spectrum, deviating by only 2-3% between theoretical and experimental frequency values. The reported vibrational motion of benzene breathing and C=C stretching (aromatic) at 740 cm^{-1} correlates well with the motion at the equivalent frequency of 750 cm^{-1} for the DFT calculations. The same behaviour is seen for p-cymene (Figure 25) where the three most intense peaks also overlap very well with the experimental values with the same 2-3% deviation of frequencies as noted with thymols spectrum. The

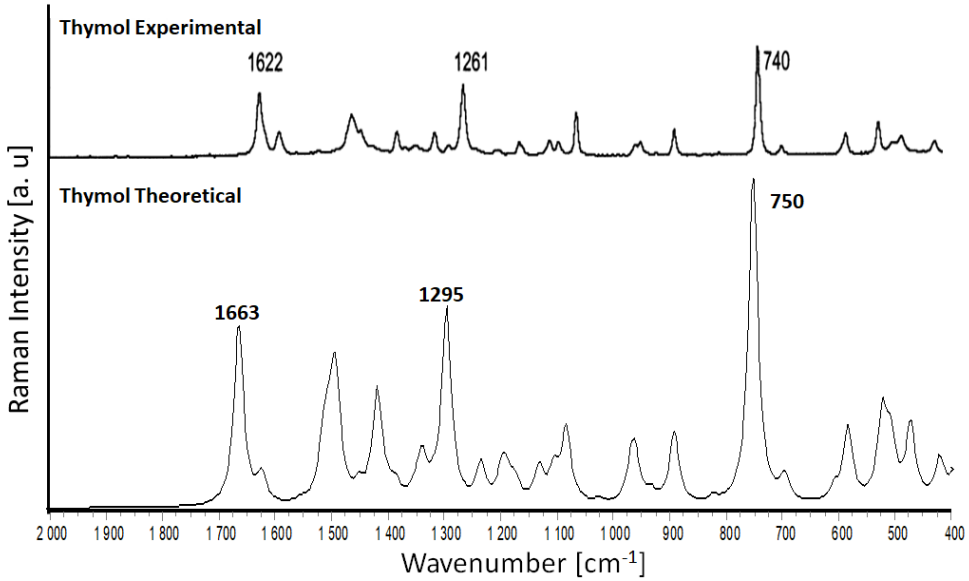

Figure 24: Comparison between experimental (top) FT-Raman spectrum taken from Schulz et al's previous work [60] and theoretical (bottom) Raman spectrum generated from my B3LYP/6-311++G(d,p) level of theory DFT calculations for thymol.

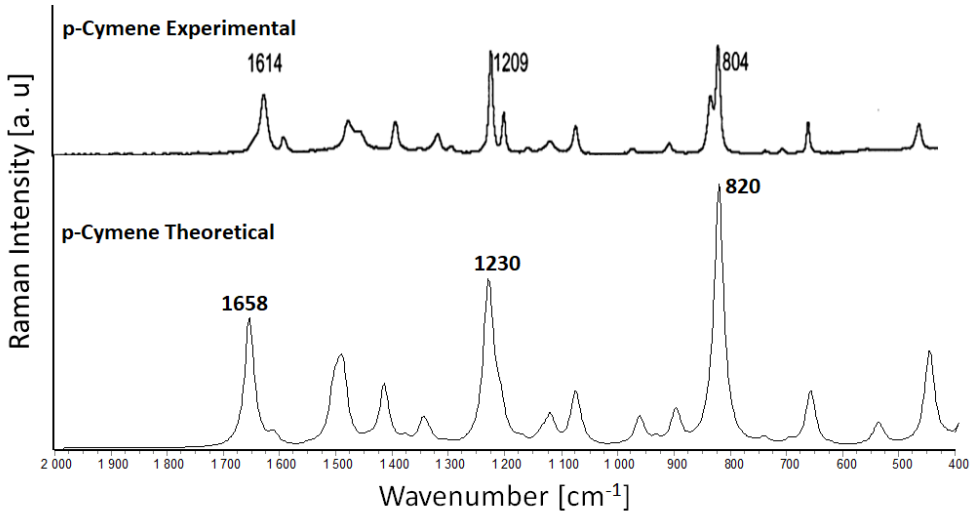

Figure 25: Comparison between experimental (top) FT-Raman spectrum taken from Schulz et al's previous work [60] and theoretical (bottom) Raman spectrum generated from B3LYP/6-311++G(d,p) level of theory DFT calculations for p-cymene.

same applies for the 804 cm^{-1} vibrational mode, where the equivalent theoretical value of 820 cm^{-1} also shows ring breathing (aromatic C=C stretching) of the benzene ring.

To summarize, the spectrum that have been data-mined from literature are in good agreement with the theoretical spectrum that have been generated at the B3LYP/6-311++g(d,p) level of calculations performed herein. This was also confirmed by the theoretical comparison with experimental spectra presented in the results section. These findings are indicative of the reliability of the calculations and provide confirmation regarding the purity of the materials employed. Moreover, they lend support to the ab initio inelastic neutron scattering (INS) spectra generated using the Mantid software, as well as affirm the vibrational characteristics of the modes described in Tables 4 and 5.

When it comes to moderation, the low energy excitations are the most important. For mesitylene these come from the free rotation of its three methyl groups [11]. Similarly to mesitylene, both p-cymene's and thymol's lowest energy vibrational modes were, according to the single molecule DFT calculations, attributed to the rotation of their methyl groups. In a separate investigation involving methyl derivatives of benzene, it was reported that the solid-state structures of toluene and m-xylene (similar to mesitylene and toluene) exhibited methyl librations that were coupled with acoustic phonon

branches characterized by low wavenumbers. These observations implied the presence of minimal external barriers impeding the rotational motion of the methyl groups. [19]. Since these chemicals are not too dissimilar to thymol and p-cymene one could assume a similar type of behaviour. The next step in assessing the efficacy of p-cymene and thymol as potential cold moderating materials would involve constructing scattering kernels for Monte-Carlo simulations, which are crucial for investigating their neutron moderating capabilities.

6 Conclusion

When searching for potential neutron moderating materials, high-resolution vibrational spectroscopy plays a pivotal role in providing essential insights into the moderating performance of the material under consideration. This is particularly true within the low energy transfer range (0 to 200 cm^{-1}) in the regime of lattice vibrations.

In this thesis, a comprehensive analysis has been conducted on the experimentally recorded and theoretically derived data associated with the INS spectra of thymol and p-cymene, both being hydrogen-rich compounds. The vibrational density of states (VDoS) of both materials has been calculated with the help of density functional theory (DFT) and characterized, with special attention to the low energy transfer range between 0 and 500 cm^{-1}.

The key takeaway from this thesis can be summarized by four points:

- The single molecule DFT calculations were verified and proven to be very precise in determining molecular vibrations. This was highlighted through comparison with experimental Raman and IR spectra, both from literature, and our own measurements.

- It has been established that the lowest energy vibrational modes, which are associated with the motion of the methyl and isopropyl groups, make both materials suitable candidates as neutron moderators.

- Both p-cymene and thymol display a lowest energy vibrational mode (23 to 26 cm^{-1}, $\approx$ 2.85 to 3.00 meV) in their crystal state, which corresponds to the free rotation of the methyl group, and could facilitate a flow of very low-energy neutrons from the materials.

- Further, p-cymene's amorphous phase displays a nice uniform distribution in the low energy transfer range of 20 to 160 cm^{-1} which could also be advantageous.

In short, using thymol, p-cymene, or a combination of the two could yield a desired VDoS for neutron moderation that is potentially superior to, or serves as an alternative to, solid methane and liquid hydrogen.

7 Perspectives

The next step in comprehensively characterizing the moderating properties of these two compounds involves the simulation of neutron energy distributions upon exiting a potential moderator containing these materials, either individually or in combinations. This can be accomplished by constructing a neutron scattering kernel, which can subsequently be employed in the simulation of the moderating process for p-cymene, thymol, and/or their mixtures using established ray-tracing software such as MCNPx, FLUKKA, NJOY, or PHITS. To construct this kernel with utmost precision, it is imperative to obtain the most accurate vibrational density of states (VDoS) and measure the total neutron scattering cross-section. Advanced density functional theory (DFT) calculations are thus warranted to achieve this goal. Theoretical inelastic neutron scattering (INS) spectra derived from DFT calculations, accessible via software tools like CRYSTAL, VASP, or CASTEP, offer enhanced support in characterizing the vibrational modes of thymol and p-cymene, particularly in the low energy transfer range where acoustic and optical modes dominate. Furthermore, the temperature-dependent total neutron scattering cross-section must be experimentally determined. The Vesuvio spectrometer at ISIS Neutron and Muon Source provides a viable means to accomplish this objective.

References

[1] F. Fernandez-Alonso and D. L. Price, *Neutron Scattering - Fundamentals* (Experimental Methods in Physical Sciences). Elsevier, 2013, vol. 44, p. 3.

[2] *Neutron lifetimes* gov. webpage. [Online]. Available: https://pdglive.lbl.gov/DataBlock.action?node=S017T.

[3] *Experimental neutron scattering*. Oxford: Oxford University Press, 2009.

[4] *ISIS Neutron and Muon Source*. [Online]. Available: https://www.isis.stfc.ac.uk/Pages/home.aspx.

[5] J. M. Carpenter and C.-K. Loong, *Elements of Slow-Neutron Scattering: Basics, Techniques, and Applications*. Cambridge: Cambridge University Press, 2015, p. 54.

[6] G. L. Squires, *Introduction to the theory of thermal neutron scattering*, 3rd ed. Cambridge: Cambridge University Press, 2012, ch. 1-2.

[7] A. Harms, *An Introduction to the CANDU Nuclear Energy Conversion System*. McMaster university, 1972, ch. 3.

[8] *Simple calculations - gjc - ill*. [Online]. Available: https://www.ill.eu/fileadmin/user_upload/ILL/3_Users/Support_labs_infrastructure/Software-tools/DIF_tools/neutrons.html.

[9] G. Škoro, G. Romanelli, S. Rudić, S. Lilley, and F. Fernandez-Alonso, "Discovery of new neutron-moderating materials at ISIS Neutron and Muon Source," *EPJ Web of Conferences*, vol. 239, p. 17 008, 2020.

[10] T. Kai, M. Harada, M. Teshigawara, N. Watanabe, and Y. Ikeda, "Coupled hydrogen moderator optimization with ortho/para hydrogen ratio," *Nuclear Instruments and Methods in Physics Research Section A: Accelerators, Spectrometers, Detectors and Associated Equipment*, vol. 523, pp. 398–414, May 2004.

[11] F. Parajón, "A Review of the Cold Neutron Moderator Materials: Neutronic Performance and Radiation Effects," *Physics Procedia*, vol. 60, pp. 219–225, 2014.

[12] M. Probert, G. Škoro, S. Rudić, *et al.*, "Spin isomers in the ISIS TS1 cryogenic hydrogen moderator," *Journal of Physics: Conference Series*, vol. 1021, no. 1, p. 012 057, May 2018.

[13] T. A. Broome, "The background to the current problems with the methane moderator," *ISIS Facility Internal Report*, 1990.

[14] D. Evans, "Irradiation effects in liquid methane used as a neutron moderator," *Cryogenics*, Nonmetallic Materials and Composites at Low Temperature-VII, vol. 35, no. 11, pp. 763–766, Nov. 1995.

[15] O. Kirichek, C. R. Lawson, D. M. Jenkins, C. J. T. Ridley, and D. J. Haynes, "Solid methane in neutron radiation: Cryogenic moderators and cometary cryo volcanism," *Cryogenics*, vol. 88, pp. 101–105, Dec. 2017.

[16] S. Tasaki, Y. Idobata, Y. Adachi, F. Funama, and Y. Abe, "Study on Moderation Properties of Cold Mesitylene using KUANS," *EPJ Web of Conferences*, vol. 231, F. Ott, A. Menelle, and C. Alba-Simionesco, Eds., p. 04 005, 2020.

[17] T. Hügle, M. Mocko, M. A. Hartl, L. L. Daemen, and G. Muhrer, "Triphenylmethane, a possible moderator material," *Nuclear Instruments and Methods in Physics Research Section A: Accelerators, Spectrometers, Detectors and Associated Equipment*, vol. 738, pp. 1–5, Feb. 2014.

[18] M. V. Bulavin, K. A. Mukhin, A. Yskakov, *et al.*, "Some Features of the Operation of Pelletized Cryogenic Mesitylene-Based Moderators at the IBR-2 Pulsed Fast Reactor," *Journal of Surface Investigation: X-ray, Synchrotron and Neutron Techniques*, vol. 16, pp. 1–6, Feb. 2022.

[19] I. Natkaniec, K. Holderna-Natkaniec, and J. Kalus, "Neutron scattering studies of methyl derivatives of benzene selected as potential materials for cold neutron moderators," *Physica B: Condensed Matter*, Proceedings of the Third European Conference on Neutron Scattering, vol. 350, E651–E653, Jul. 2004.

[20] M. F. Nagoor Meeran, H. Javed, H. Al Taee, S. Azimullah, and S. K. Ojha, "Pharmacological Properties and Molecular Mechanisms of Thymol: Prospects for Its Therapeutic Potential and Pharmaceutical Development," *Frontiers in Pharmacology*, vol. 8, 2017.

[21] G. Škoro, G. Romanelli, S. Rudić, S. Lilley, and F. Fernandez-Alonso, "Discovery of new neutron-moderating materials at isis neutron and muon source," *EPJ Web of Conferences*, vol. 239, Z. Ge, N. Shu, Y. Chen, W. Wang, and H. Zhang, Eds., p. 17 008, 2020.

[22] A. Das and T. Ferbel, *Introduction to nuclear and particle physics*, 2nd ed. New Jersey: World Scientific, 2009, ch. 1-2.

[23] W. M. Stacey, *Nuclear Reactor Physics*, 2nd ed. Weinheim: Wiley-VCH, 2007.

[24] D. L. Price, "Neutrons and solid state physics," *Physics Today*, vol. 48, no. 9, pp. 93–94, 1995.

[25] *Neutron Scattering Lengths and cross sections*. [Online]. Available: https://www.ncnr.nist.gov/resources/n-lengths/elements/h.html.

[26] J. Barnert, *Conceptual design of a cold methane moderator system for the European Spallation Source (ESS)*.

[27] H. S. Camarda, "Monte Carlo studies of D2O and H2O neutron moderators for time of flight experiments," *Nuclear Instruments and Methods*, vol. 106, no. 2, pp. 205–212, 1973.

[28] D. A. McQuarrie, *Statistical mechanics*. Sausalito, Calif: University Science Books, 2000, ch. 7.

[29] D. Sivia, *Elementary Scattering Theory: for X-ray and Neutron users*. Oxford: Oxford University Press, 2011, ch. 3.

[30] R. Pynn, "Neutron Scattering—A Non-destructive Microscope for Seeing Inside Matter," in *Neutron Applications in Earth, Energy and Environmental Sciences*, I. S. Anderson, A. J. Hurd, R. L. McGreevy, L. Liang, R. Rinaldi, and H. Schober, Eds., Boston, MA: Springer US, 2009, pp. 15–36.

[31] I. Grillo, "Small-Angle Neutron Scattering and Applications in Soft Condensed Matter," in *Soft Matter Characterization*, R. Borsali and R. Pecora, Eds., Dordrecht: Springer Netherlands, 2008, pp. 723–782.

[32] J. M. de Souza, P. T. C. Freire, D. N. Argyriou, *et al.*, "Raman and neutron scattering study of partially deuterated l-alanin: Evidence of a solid-solid phase transition," *ChemPhysChem*, vol. 10, no. 18, pp. 3337–3343, 2009.

[33] K. Y. S. M. Girvin, "Modern condensed matter physics," in *Modern Condensed Matter Physics*, 1st ed. United Kingdom: Cambridge University Press, 2019, pp. 78–96.

[34] J. J. Sakurai, "Advanced quantum mechanics," in 4th ed. 2008. Berlin, Heidelberg: Springer Berlin Heidelberg, 2008.

[35] K. Wang, Y. Chen, M. Kadic, C. Wang, and M. Wegener, "Nonlocal interaction engineering of 2D roton-like dispersion relations in acoustic and mechanical metamaterials," *Communications Materials*, vol. 3, pp. 1–11, May 2022.

[36] B. S. Hudson, "Inelastic Neutron Scattering: A Tool in Molecular Vibrational Spectroscopy and a Test of ab Initio Methods," *The Journal of Physical Chemistry A*, vol. 105, no. 16, pp. 3949–3960, Apr. 2001.

[37] S. F. Parker, "Vibrational Spectroscopy with Neutrons," in *Encyclopedia of Biophysics*, G. C. K. Roberts, Ed., Berlin, Heidelberg: Springer, 2013, pp. 2729–2734.

[38] J. C. Smith, P. Tan, L. Petridis, and L. Hong, "Dynamic Neutron Scattering by Biological Systems," *Annual Review of Biophysics*, vol. 47, no. 1, pp. 335–354, May 2018.

[39] K. Dymkowski, S. F. Parker, F. Fernandez-Alonso, and S. Mukhopadhyay, "AbINS: The modern software for INS interpretation," *Physica B: Condensed Matter*, vol. 551, pp. 443–448, 2018.

[40] W. Kołos and L. Wolniewicz, "Nonadiabatic theory for diatomic molecules and its application to the hydrogen molecule," *Reviews of modern physics*, vol. 35, no. 3, pp. 473–483, 1963.

[41] S. F. Sousa, P. A. Fernandes, and M. J. Ramos, "General Performance of Density Functionals," *The Journal of Physical Chemistry A*, vol. 111, no. 42, pp. 10 439–10 452, Oct. 2007.

[42] A. J. Cohen, P. Mori-Sánchez, and W. Yang, "Challenges for Density Functional Theory," *Chemical Reviews*, vol. 112, no. 1, pp. 289–320, Jan. 2012.

[43] A. D. Becke, "Perspective: Fifty years of density-functional theory in chemical physics," *The Journal of Chemical Physics*, vol. 140, Apr. 2014.

[44] H. Bukheet, "Density function theory b3lyp/6-31g**calculation of geometry optimization and energies of donor-bridge-acceptor molecular system," vol. 44, Sep. 2014.

[45] V. Gupta, "Introduction and overview," en, in *Molecular and Laser Spectroscopy*, Elsevier, 2020, pp. 1–40.

[46] S. Corsetti, D. McGloin, and J. Kiefer, "Comparison of Raman and IR spectroscopy for quantitative analysis of gasoline/ethanol blends," *Fuel*, vol. 166, pp. 488–494, Feb. 2016.

[47] H. W. Siesler, "Vibrational Spectroscopy," in *Reference Module in Materials Science and Materials Engineering*, Elsevier, Jan. 2016, pp. 10–15.

[48] R. S. Pinna, S. Rudić, S. F. Parker, *et al.*, "The neutron guide upgrade of the TOSCA spectrometer," *Nuclear Instruments and Methods in Physics Research Section A: Accelerators, Spectrometers, Detectors and Associated Equipment*, vol. 896, pp. 68–74, Jul. 2018.

[49] S. F. Parker, F. Fernandez-Alonso, A. J. Ramirez-Cuesta, *et al.*, "Recent and future developments on TOSCA at ISIS," *Journal of Physics: Conference Series*, vol. 554, p. 012 003, Nov. 2014.

[50] R. S. Pinna, S. Rudić, S. F. Parker, G. Gorini, and F. Fernandez-Alonso, "Monte carlo simulations of the TOSCA spectrometer: Assessment of current performance and future upgrades," *EPJ Web of Conferences*, vol. 83, p. 03 013, 2015.

[51] A. Perrichon, C. Bovo, S. F. Parker, D. Raspino, J. Armstrong, and V. García Sakai, "Overview of planned upgrade to the secondary spectrometer of TOSCA," *Nuclear Instruments and Methods in Physics Research Section A: Accelerators, Spectrometers, Detectors and Associated Equipment*, vol. 1047, p. 167 899, 2023.

[52] D. Colognesi and F. Tasset, "TOSCA neutron spectrometer: The final configuration," *Applied Physics A*, vol. 74, no. s1, pp. 23–26,

[53] Jmol development team, *Jmol*, version 14.6.4, Oct. 7, 2016. [Online]. Available: http://jmol.sourceforge.net/.

[54] M. J. Frisch, G. W. Trucks, H. B. Schlegel, *et al.*, *Gaussian16 revision c.01*, Gaussian, Inc., Wallingford CT, 2016.

[55] *Overview — SCARF User Documentation 0.1 documentation*. [Online]. Available: https://www.scarf.rl.ac.uk/.

[56] O. Arnold, J. C. Bilheux, J. M. Borreguero, *et al.*, "Mantid—Data analysis and visualization package for neutron scattering and SR experiments," *Nuclear Instruments and Methods in Physics Research Section A: Accelerators, Spectrometers, Detectors and Associated Equipment*, vol. 764, pp. 156–166, Nov. 2014.

[57] *Chemcraft - Graphical program for visualization of quantum chemistry computations*. [Online]. Available: https://www.chemcraftprog.com/.

[58] A. Thozet and M. Perrin, "Structure of 2-isopropyl-5-methylphenol (thymol)," *Acta Crystallographica Section B*, vol. 36, no. 6, pp. 1444–1447,

[59] P. Rajkumar, S. Selvaraj, R. Suganya, D. Velmurugan, S. Gunasekaran, and S. Kumaresan, "Vibrational and electronic spectral analysis of thymol an isomer of carvacrol isolated from Trachyspermum ammi seed: A combined experimental and theoretical study," *Chemical Data Collections*, vol. 15-16, pp. 10–31, Aug. 2018.

[60] H. Schulz, M. Baranska, R. Quilitzsch, and W. Schütze, "Characterisation of essential oil plants from Turkey by IR and Raman spectroscopy," *Vibrational Spectroscopy*, vol. 39, no. 2, pp. 249–256, 2005.

[61] H. Kjær and S. P. A. Sauer, "Pople Style Basis Sets for the Calculation of NMR Spin–Spin Coupling Constants: The 6-31G-J and 6-311G-J Basis Sets," *Journal of Chemical Theory and Computation*, vol. 7, no. 12, pp. 4070–4076, Dec. 2011.

[62] A. J. R.-C. P C. H. Mitchell S. F. Parker, *Vibrational spectroscopy with neutrons with applications in chemistry, biology, materials science and catalysis* (Series on neutron techniques and applications ; vol. 3). Hackensack, NJ: World Scientific, 2005.

Appendix A

Density Functional Theory

Quantum mechanical calculations revolve around finding solutions that satisfy the Schrodinger equation. More specifically the time independent Schrodinger equation:

$$\hat{H}\Psi = E\Psi \tag{25}$$

The wavefunction Ψ gives a lot of information about molecular systems. Their potential energies, the most stable geometries as well as their vibrational electronic energy levels.

$\hat{H}$ is the Hamiltonian operator. The Hamiltonian is a differential operator which represents the total energy of the system; the potential and kinetic energies.

Ψ_n is a set of eigen functions with associated eigenvalues E_n, that satisfy the Hamiltonian. Each of the solutions are referred to as eigen states. The detailed definition of the Hamiltonian depends on the system being described using the Schrodinger equation. Some well known examples of this includes the particle in a box and the simple harmonic oscillator. In these examples the Hamiltonian adopts a simple form and in this simplified form the equation can be solved exactly. However, this is not the case for more complex systems, such as molecules and surfaces. Since these systems have many interacting parts that scale in complexity with the number of electrons and nuclei in the system. In such a system , consisting of M nuclei and N electrons in the absence of an external magnetic or electric field, the Hamiltonian may take the form:

$$\hat{H} = -\frac{1}{2}\sum_{i=1}^{N}\nabla_i^2 - \frac{1}{2}\sum_{A=1}^{M}\frac{1}{M_A}\nabla_A^2 - \sum_{i=1}^{N}\sum_{A=1}^{M}\frac{Z_A}{r_{iA}} + \sum_{i=1}^{N}\sum_{j>1}^{N}\frac{1}{r_{ij}} + \sum_{A=1}^{M}\sum_{B>A}^{M}\frac{Z_A Z_B}{R_{AB}} \tag{26}$$

Here the equation is made simple using a system of atomic units with physical quantities being expressed as multiples of fundamental constants and or combinations of these. The mass of the electron, Planck's constant as well as the permittivity of free space are all set to unity. Particle mass charge and action are all expressed as multiples of these constants and can therefore be dropped from the equation. Indices A and B denote the M nuclei of the system whilst i and j denote the N electrons of the system. The other parameters are as follows; M_A the mass of nuclei A, Z_A the charge of nuclei A, r denotes either the distance between an electron and an electron,

i.e. i to j, or the distance between electron and nuclei, whilst R denotes the distance between nuclei A and B. The first two parts of the equation are used to describe the systems kinetics and the other 3 parts describe the systems potentials.

This is where the complexity reveals itself as one needs to consider all possible interactions between electrons and nuclei simultaneously. One approximation that helps reduce the equations complexity, the Born-Oppenheimer approximation, makes use of the observation that electrons and nuclei differ in mass by 3 orders of magnitude. Take the velocity, v:

$$v = \sqrt{\frac{2E_{KE}}{m}} \tag{27}$$

and imagine transferring some amount of kinetic energy to an electron and a nuclei. From the perspective of electrons nuclei seem static in comparison, but from the nucleus's perspective the electrons seem to be whizzing by. Using this observation the Hamiltonian can be simplified by splitting it into two parts a nuclear and an electronic part, which can be solved separately. The electronic part can first be solved by treating the nuclei as fixed with respect to the electrons this part is solved repeatedly in small steps, thus allowing the mapping of electrons as a function of the nuclei coordinates to produce a potential energy surface. The nuclear part can then be solved separately using this potential energy surface calculated for the electronic part. It is this decoupling of the equation into electronic and nuclear parts that is called the Born-Oppenheimer approximation. Rewriting the Hamiltonian from equation 21 using this approximation results in:

$$\hat{H} = -\frac{1}{2}\sum_{i=1}^{N}\nabla_i^2 - 0 - \sum_{i=1}^{N}\sum_{A=1}^{M}\frac{Z_A}{r_{iA}} + \sum_{i=1}^{N}\sum_{j>1}^{N}\frac{1}{r_{ij}} + const \tag{28}$$

Since the nuclei are approximated as static the part describing their kinetic energy may be dropped (set to 0 in the above equation). Furthermore, the nuclear nuclear repulsion becomes a constant and is dropped from this reduced Hamiltonian resulting in an "electronic Hamiltonian":

$$\hat{H} = -\frac{1}{2}\sum_{i=1}^{N}\nabla_i^2 - \sum_{i=1}^{N}\sum_{A=1}^{M}\frac{Z_A}{r_{iA}} + \sum_{i=1}^{N}\sum_{j>1}^{N}\frac{1}{r_{ij}} = \hat{T} + \hat{V}_{NE} + \hat{V}_{ee} \tag{29}$$

Where T is the kinetic energy, V_{NE} the electrostatic attraction between electron and nuclei and V_{ee} the electron electron electrostatic repulsion. Most

systems can be approximately described entirely by this electronic Hamiltonian.

Solutions to the Schrodinger equation using this electronic Hamiltonian is the electronic wave function and its associate eigenvalue.

$$\hat{H}_{elec}\Psi_{elec}(\vec{r}_1, ..., \vec{r}_N) = E_{elec}\Psi_{elec}(\vec{r}_1, ..., \vec{r}_N) \tag{30}$$

The electronic wavefunction Ψ_{elec} is a function of the electron position $\vec{r}_i$ only. Though, a complete description must also take the spin of electrons into account. Solving Ψ_{elec} that yields the lowest eigenvalue, E_{elec} is the ground state energy of the system. However, even with the applied approximation, solving Schrodinger's equation is no trivial matter as the part of the electronic Hamiltonian that describes electrostatic repulsion between electrons still remains a many body problem as each electron experiences the electrostatic repulsion of each other electron simultaneously. To get past this problem an approximation needs to be made. The solution is density functional theory (DFT). By expressing the electrostatic repulsion potential as a function of density we can vastly reduce the computing power of the calculations. Instead of considering 3N interactions, with N being the number of electrons, we can express this electrostatic repulsion by just 3 parameters, x, y and z. This is made possible through the Kohn-Hohenberg theorem. This theorem states there there exists a one to one relationship between the ground state wave function and the electron density. This means that the ground state energy can be expressed as a function of the electron density.

It is useful to state the energy in terms of single electron wave functions. The complete energy functional is composed of two parts:

$$E[\Psi_i] = E_{known}[\Psi_i] + E_{XC}[\Psi_i] \tag{31}$$

a known part, $E_{known}[\Psi_i]$, and an exchange correlation factor, $E_{XC}[\Psi_i]$. The known part contains the sum of all parts that can be written down in an analytical form whilst everything else is contained within the exchange correlation factor of the energy function. The known term includes four contributions:

$$E_{known}[\Psi_i] = \sum_i \int \Psi_i^* \nabla^2 \Psi_i d^3r + \int V(\vec{r}) n(\vec{r}) d^3r \tag{32}$$

$$+\frac{1}{2}\int\int \frac{n(\vec{r})n(\vec{r}')}{|\vec{r} - \vec{r}'|} d^3r d^3r' + E_{ion} \tag{33}$$

the first one described the kinetic energies , the second the coulomb interaction between electrons and nuclei, the third is the coulomb interactions

between pairs of electrons and finally the fourth term is the coulomb interaction between pairs of nuclei. The exchange correlation part, E_{XC}, of equation 31 is a placeholder for all the hard to describe effects not included in the known term, such as quantum mechanical interpretations.

But how do we go about solving equation 31? Kohn and Sham showed that finding the right electron density can be done through solving a set of equations of the form:

$$[\frac{1}{2}\nabla^2 + V(\vec{r}) + V_H(\vec{r}) + V_{XC}(\vec{r})]\Psi_i(\vec{r}) = \epsilon_i\Psi_i(\vec{r}) \tag{34}$$

with each equation involving only a single electron. We can see that the expression closely resembles the electronic Hamiltonian (equation 29). The key difference is that the summations are dropped in the Kohn-Sham equation of the full Schrodinger equation. This is because solutions to the Kohn-Sham equations are single electron wave functions that depend only on the three spatial variables, x ,y and z. The first part of the Kohn-Sham equation describes the kinetic energy of an electron, while the other three terms describe the potentials. The first potential term in equation **??**, $V(\vec{r})$, also appears in the full Schrodinger equation and describes the interaction between electrons and nuclei. The second potential term, $V_H(\vec{r})$, is coined the Hartree potential. This term describes the coulombic repulsion between the electron being considered and all other electrons in the system.

$$V_H(\vec{r}) = \int \frac{n(\vec{r'})}{|\vec{r} - \vec{r'}|} \tag{35}$$

An issue that arises from the Hartree potential is that the term also includes the repulsion between the considered electron and itself which is not a physical result and is an undesired contribution. Corrections to this are usually what would be included in the exchange correlation term in the complete energy functional, equation **??**.

$$V_{XC}(\vec{r}) = \frac{\delta E_{XC}(\vec{r})}{\delta n(\vec{r})} \tag{36}$$

Due to the process of solving these equation appearing circular, i.e to solve the Kohn-Sham equations require that one defines the Hartree potential. But in order to define the Hartree potential the electron density needs to be defined. However, to define the electron density requires knowing the single electron wave functions. But in order to know the single electron wave functions one must first solve the Kohn-Sham equations. The way this circular behaviour is counteracted is by treating the problem in an iterative fashion and involves following a procedure of:

- Defining an initial, trial electron density, $(n(\vec{r}))$
- Solving the Kohn-Sham equations using this trial density to find the single-particle wave function $(\Psi_i(\vec{r}))$
- Calculating the electron density defined by the single-particle wave functions from above, $n_{ks}(\vec{r}) = 2\sum_i \Psi_i^*(\vec{r})\Psi_i(\vec{r})$
- Finally compare the calculated electron density with that of the trial electron density from step 1. If these densities are "similar", this is then the ground-state electron density. Otherwise update that trial electron density and the procedure is repeated.

However, a complete solution of the Kohn-Sham equations still requires that one specifies the exchange correlation functional. This is, unfortunately, not possible as it is not "known" as such and must again be approximated. There is one case where it can be derived exactly, namely, for a uniform electron gas.

The most common approximations for the exchange correlation functional are the local density approximations (LDA):

$$V_{XC}(\vec{r}) = V_{XC}^{electrongas}[n(\vec{r})] \tag{37}$$

In these approximation we treat the electron density as being constant in all points in space. This might not seem too practical since it is the variations in electron density that are interesting. Though, the main goal of LDA is to provide a practical solution to the Kohn-Sham equations. The way this works in practice is by substituting the exchange correlation potential of equation **??** by the exchange correlation potential of a uniform electron gas at the electron density in that position. Form of exchange for a uniform electron gas (UEG):

$$E_x^{LDA} = -\frac{3}{4}\left(\frac{3}{\pi}\right)^{1/3}\int \rho^{4/3} dr \tag{38}$$

Gradient expansion approximation for a UEG:

$$E_x^{LDA} = -\int \rho^{4/3}\left[\frac{3}{4}\left(\frac{3}{\pi}\right)^{1/3} + \frac{7}{432\pi(\pi^2)^{1/3}}x^2 + ...\right] dr \tag{39}$$

To encompass all variable formulations specific to each field making use of the DFT. The generalized gradient approximation:

$$E_x^{GGA}(p,x) = \int \rho^{4/3} F(x) dr \tag{40}$$

Where F(x) can be chosen to obey the gradient expansion in the low x-limit. Note, x is the dimensionless reduced gradient:

$$x = |\nabla\rho|/\rho^{4/3} = 2(3\pi^2)^{1/3} s \tag{41}$$

and not a measure of distance. The most commonly used GGA type exchange functionals are B88

$$E_x^{B88} = -\sum_{\sigma=\alpha,\beta} \int \rho_\sigma^{4/3} \left[\frac{3}{4} \left(\frac{6}{\pi} \right)^{1/3} + \frac{\beta x_\sigma^2}{1 + 6\beta x_\sigma sinh^{-1} x_\sigma} \right] dr \tag{42}$$

and PBE:

$$E_x^{PBE} = -\int \rho^{4/3} \left[\frac{3}{4} \left(\frac{3}{\pi} \right)^{1/3} + \frac{\mu s^2}{1 + \mu s^2/\kappa} \right] dr \tag{43}$$

The developement of correlation functionals for LDA are far more complex, taking longer to develope. The two well established functionals are LYP and PBE. There exists a plethora of exchange-correlation DFT's, LDA, GGA, meta-GGA among others have been developed over time. The last clear advance in developing exchange-correlation functionals came with the inclusion of Hartree-Fock exchange (HF):

$$E_x^{HF} = -\frac{1}{2} \sum_{i,j,\sigma} \int \int \frac{\phi_{i\sigma}^*(r)\phi_{j\sigma}(r)\phi_{j\sigma}^*(r')\phi_{i\sigma}(r')}{|r - r'|} dr dr' \tag{44}$$

Axel Becke came with the idea, through the adiabatic connection (energy transfer through work) that the functional should contain some E_x^{HF}. He proposed a linear model that mixes some correlation functionals with some local DFA exchange:

$$E_{xc}^{BHH} = \frac{1}{2} E_x^{HF} + \frac{1}{2} W_1^{LDA} \tag{45}$$

This model gave rise to functionals such as BHLYP. BHLYP did not generally perform better than GGA-type functionals, but did provide to be a valuable precursor to the next step. Introducting some experimental data to build upon the idea, resulting in:

$$E_{xc}^{B3} = aE_x^{HF} + (1-a)E_x^{LDA} + b\nabla E_x^{B88} + cE_c^{GGA} + (1-c)E_c^{LDA} \tag{46}$$

The three parameters a, b and c were fitted to experimental data resulting in the B3LYP functional as implemented in GAUSSIAN (software used in computational chemistry) [54]:

$$E_{xc}^{B3LYP} = 0.2E_x^{HF} + 0.8E_x^{LDA} + 0.72\nabla E_x^{B88} + 0.81E_c^{LYP} + 0.19E_c^{VWN} \quad (47)$$

Which is to today's date the most commonly used, as well as most precise, functional used in computation chemistry[41]–[44].

Basis Sets

Basis sets are generically just collections of vectors that span the space within the scope of the problem being solved. For a 3D linear vector space in Cartesian coordinates $\hat{i}, \hat{j}, \hat{k}$ are used to define these vectors.

In Quantum Chemistry

here "basis sets" refer to the set of non-orthogonal one-particle functions used to build molecular orbitals. Other theorists might mention "N-electron basis sets" which is something very different and refers to sets of Slater determinants.

LCAO-MO Approximation

Molecular orbitals (MO's) are build from linear combinations of atomic orbitals (AO's). AO's are most often represented by gaussians in quantum chemistry calculations. Furthermore, AO's simply refer to functions centered around atoms.

Gaussian-Type Orbitals

Gaussian-Type Orbitals (GTO's) take the form:

$$\phi_{abc}^{GTO}(x, y, z) = Nx^a y^b z^c e^{-\zeta r^2} \quad (48)$$

Here a,b and c control angular momentum: $L = a + b + c$ and ζ controls orbital width. These type of functions are much easier to compute since the product of two ore more Gaussian's simply result in another Gaussian.

Contracted GTO's

Contracted GTO's, or CTGO's, are an approximation of Slater-type orbitals (STO's), which a more accurate, constructed by a linear combination of regular GTO's. This mimicking of STO's is often called an "STO-nG" basis set, despite it being constructed by GTO's.

$$\phi_{abc}^{CGTO}(x,y,z) = N\sum_{i=1}^{n} c_i x^a y^b z^c e^{-\zeta_i r^2} \tag{49}$$

Where c_i is a "contraction"-coefficient and is fixes as per defined by the basis set. An STO-2G and STO-3G basis set would refer to 2 and 3 gaussians that are used to mimic an STO.

Types of Basis Sets

- Minimal: One basis function (STO,GTO or CGTO) for each atomic orbital in the atom.
- Double-zeta: two basis functions for each AO.
- Triple-zeta: Three basis functions for each AO etc... until 6-zeta.
- Split-valence: Uses one basis function for each core AO and larger basis for valence AO's.

I general, the more basis functions we use to linearly combine into a MO's, the more accurate the calculations will be.

Alphabet Principle

Writing down the electron configuration for carbon would go as follows $1S_2 2S_2 2P_2$. How many minimum basis functions would be needed for a minimum basis set? For the S-orbitals we can get away with a single function for each, but for the p-orbitals we have 3 minimum functions that are necessary. One for $2P_x, 2P_y$ and $2P_z$. This holds true for d-orbitals as well, which would need 5 functionals to be constructed.

Example Atom Types

- H-atom minimal basis: One 1S AO, one basis function.
- C-atom minimal basis: 1S, 2S, $2P_x, 2P_y$ and $2P_z$ AO's. So 5 basis functions are necessary.

Table 6: STO-3G example for H-atom

H	0		
S	3	1.00	
		ζ_i	c_i
		3.425	0.154
		0.624	0.535
		0.169	0.444

An example of how a STO-3G basis set for hydrogen would look like using the GAUSSIAN-type file format. This table would usually only contain the numbers, but ζ_i and c_i are included here to aid the reader in understanding the formatting.

- C-atom, double zeta: Two basis functions per AO with a total of 10 AO's
- C-atom, split valence, double-zeta: 9 basis functions, since we have one core function for our 1S.

Computing Basis Functions

Basis functions with a basis set that includes CGTO's are counted as a single function. However, the primitive GTO function inside the CGTO are not counted as basis functions. Fx. in a 6-31G* basis, carbon has one "basis function" representing the 1S orbital and not 6.

Polarization functions

Take the following situation: An atom is moving into proximity of our reference atom. The orbitals would likely want to respond due to the electromagnetic field the atom-in-motion produces and the electron density would shift in response to this, resulting in polarization. S-orbitals can only polarize if mixed with a P-orbital and P-orbitals can only polarize if mixed with a d orbital and so on. This results in "polarized" ζ-functions.

Anatomy of a Basis Set: H-atom STO-3G

A basis set of CGTO's needs to specify the exponents (ζ_i) and the contraction coefficients, c_i. An example of this is presented in table 6 in the format of GAUSSIAN.

So, a STO-3G basis set for a hydrogen atom would consist of a CGTO comprised of 3 Gaussian. Table 7 shows the same format, but for a carbon atom instead of a hydrogen. Notice how the s and p orbitals share the same ζ_i but have different values of c_i for the s and p orbital functions.

Table 7: STO-3G example for C-atom

C	0			
S	3	1.00		
		ζ_i	c_i, s	c_i, p
		71.616	0.154	
		13.045	0.535	
		3.531	0.445	
SP	3	1.00		
		2.941	-0.099	0.156
		0.683	0.399	0.607
		0.222	0.700	0.392

An example of how a STO-3G basis set for carbon would look like using the GAUSSIAN-type file format. This table would usually only contain the numbers, but ζ_i, c_i, s and c_i, p are included here to aid the reader in understanding the formatting.

Pople Basis Sets

STO-3G is a minimal basis set wherein each individual AO is represented by 3 gaussians, in order to mimic an STO. Pople's split-valence double-zeta basis set is called 6-31G and consists of a core orbital CGTO constructed from 6 Gaussian and the with the valence being described by two orbitals; one CGTO constructed from 3 gaussians and one from a simple gaussian (see table 8)[61].

More on Pople Basis Sets

fx. 6-31G* (or alternatively 6-31G(d)) is 6-31G with added d-polarization functions on non-hydrogen atoms; 6-31G** (or alternatively 6-31G(d,p)) is 6-31G* with added p-polarization functions for hydrogen.

Table 8: 6-31G example for a C-atom

C	0			
S	6	1.00		
		ζ_1	c_1	
		ζ_2	c_2	
		ζ_3	c_3	
		ζ_4	c_4	
		ζ_5	c_5	
		ζ_6	c_6	
SP	3	1.00		
		ζ_7	c_7, s	c_7, p
		ζ_8	c_8, s	c_8, p
		ζ_9	c_9, s	c_9, p
SP	1	1.00		
		$\zeta_1 0$	c_{10}, s	c_{10}, p

An example of how a STO-3G basis set for carbon would look like using the GAUSSIAN-type file format. This table would usually only contain the numbers, but ζ_i, c_i, s and c_i, p are included here to aid the reader in understanding the formatting.

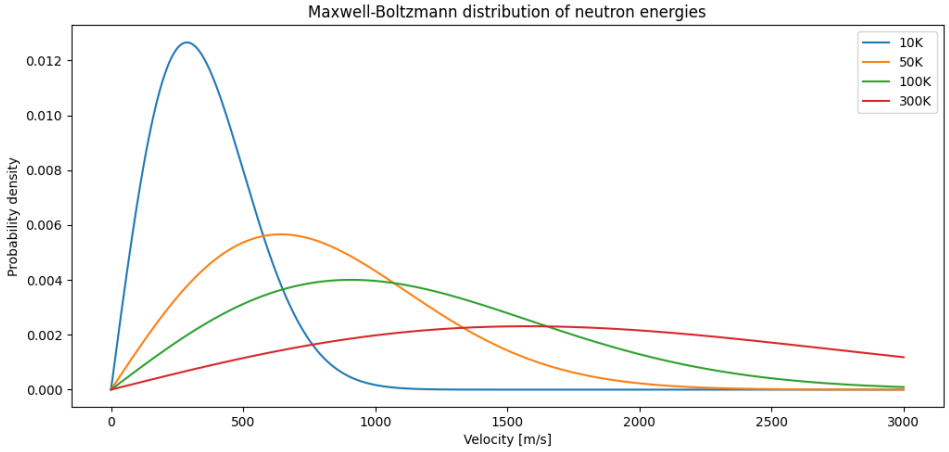

Figure 26: Probability distribution of neutron velocities, as they exit a theoretical hydrogen moderator, calculated from a Maxwell-Boltzmann distribution, given as a function of temperature.

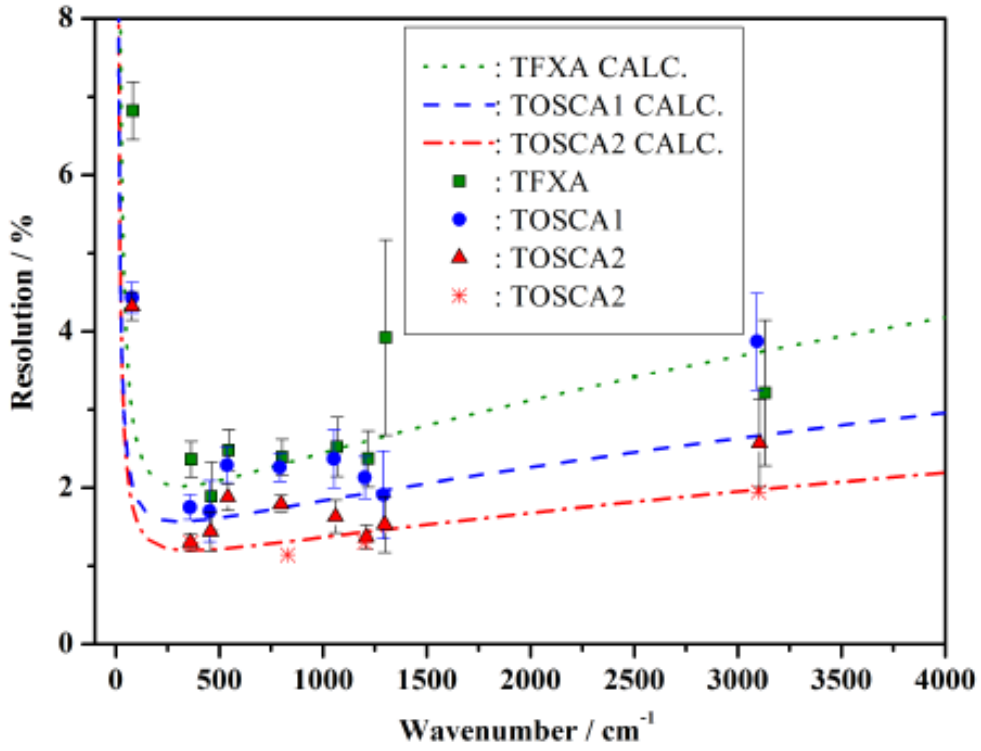

Figure 27: Resolution spectra of TFXA, TOSCA-I and TOSCA-II. The lines represent the analytical calculations. Taken from [62].

Appendix B

Full Spectra & Data

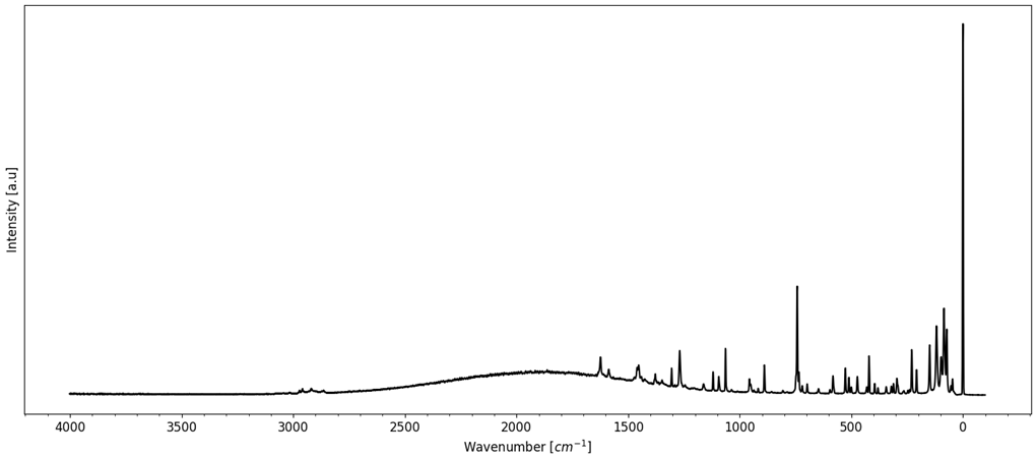

Figure 28: Experimental Raman spectrum of thymol recorded with the use of a 785 nm laser at a temperature of 6 K.

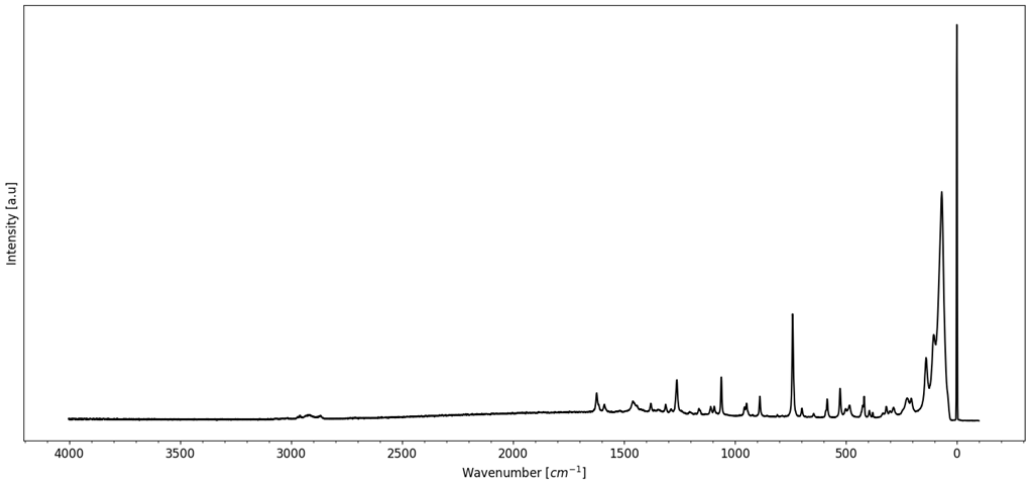

Figure 29: Experimental Raman spectrum of thymol recorded with the use of a 785 nm laser at a temperature of 298 K.

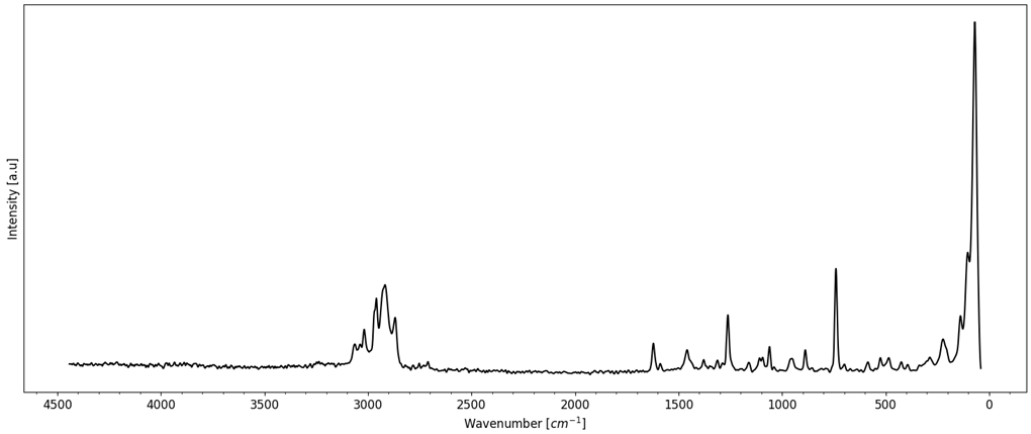

Figure 30: Experimental Raman spectrum of thymol recorded with the use of a 532 nm laser at a temperature of 298 K.

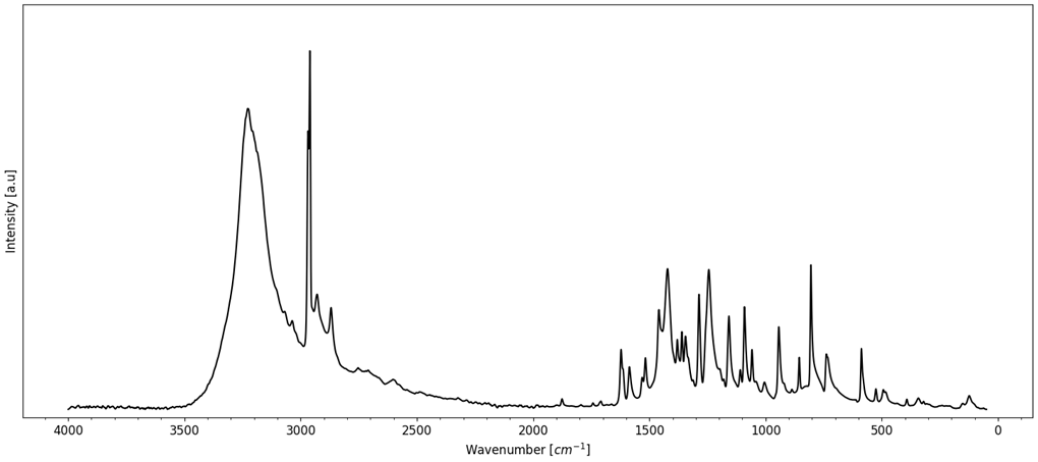

Figure 31: Experimental FT-IR spectrum of thymol recorded at a temperature of 298 K.

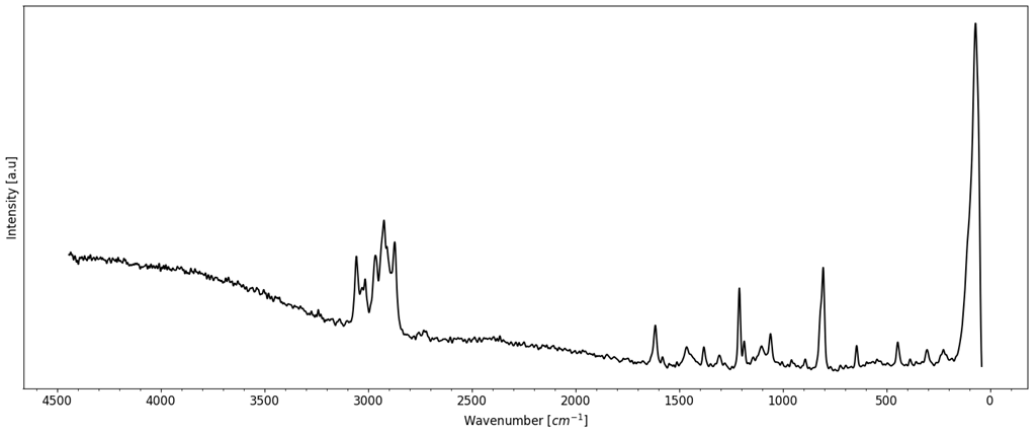

Figure 32: Experimental FT-Raman spectrum of p-cymene recorded with the use of a 532 nm laser at a temperature of 298 K.

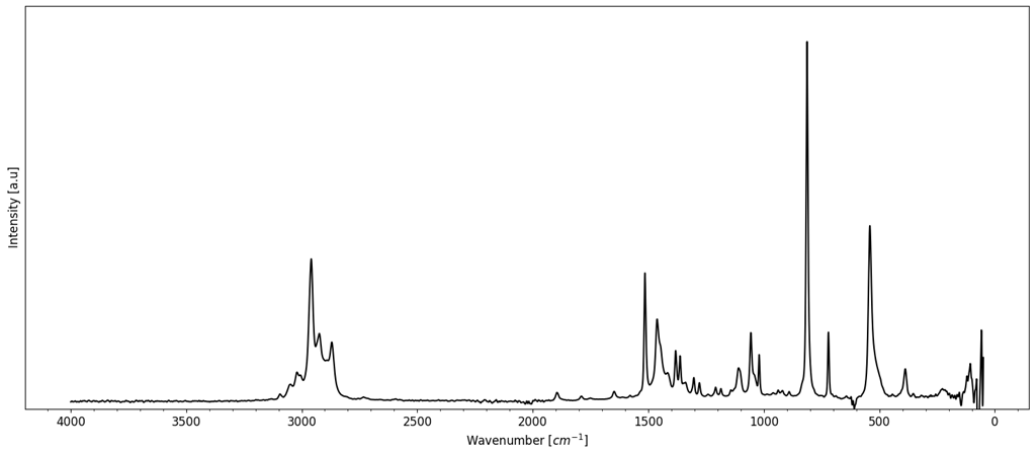

Figure 33: Experimental FT-IR spectrum of p-cymene recorded at a temperature of 298 K.

Table 9: Calculated frequencies and IR intensities of p-cymene from B3LYP/6-31++G(d,p) calculations

Freq. (cm^{-1})	IR int. (a.u.)	Freq. (cm^{-1})	IR int. (a.u.)	Freq. (cm^{-1})	IR int. (a.u.)
31.55	0.21	38.52	0.06	94.16	0.86
188.78	0.22	212.98	0.37	234.38	0.11
259.13	0.14	290.69	0.1	354.9	0.13
386.43	1.08	418.16	0.0	445.84	0.12
535.03	0.17	549.7	21.62	655.58	0.04
694.9	0.18	737.06	4.58	819.24	0.72
833.58	33.86	850.01	0.02	897.75	0.46
930.78	0.48	959.66	0.31	961.67	0.11
976.16	0.0	1005.39	0.08	1034.57	3.93
1062.33	9.2	1075.95	13.03	1120.39	1.19
1137.2	7.19	1173.58	1.22	1211.08	0.72
1231.24	3.03	1237.24	0.2	1314.79	4.71
1341.72	0.31	1344.01	2.32	1381.09	4.11
1402.21	5.89	1419.72	0.18	1422.62	3.4
1448.59	1.82	1490.97	0.0	1492.67	7.12
1494.48	3.07	1497.85	13.44	1506.32	7.22
1511.73	6.48	1550.96	25.36	1618.03	0.29
1662.58	0.34	3025.0	18.13	3029.56	43.63
3030.23	31.54	3034.67	35.88	3087.37	20.56
3096.09	0.09	3102.01	86.83	3108.71	22.61
3110.52	34.71	3114.69	18.37	3161.91	17.26
3164.32	11.41	3179.3	37.61	3184.42	9.57

Frequencies and intensities rounded off to 2 decimal points.

Table 10: Calculated frequencies and IR intensities of p-cymene from B3LYP/6-311++G(d,p) calculations

Freq. (cm^{-1})	IR int. (a.u.)	Freq. (cm^{-1})	IR int. (a.u.)	Freq. (cm^{-1})	IR int. (a.u.)
23.09	0.18	37.96	0.04	93.99	0.85
187.93	0.25	212.16	0.31	233.79	0.1
257.72	0.11	290.6	0.11	355.07	0.2
385.59	1.25	416.81	0.02	445.46	0.13
535.92	0.1	549.13	23.32	656.66	0.04
694.06	0.21	739.21	4.37	819.71	0.43
833.67	33.83	846.95	0.03	896.05	0.42
930.54	0.51	958.22	0.4	960.81	0.1
977.79	0.0	1002.78	0.25	1036.46	3.92
1060.83	6.64	1074.35	15.51	1119.14	1.34
1134.36	7.28	1171.07	1.1	1208.27	0.84
1228.3	3.48	1235.75	0.04	1306.11	2.89
1334.73	1.97	1344.69	2.22	1376.49	3.08
1397.52	6.68	1414.04	0.42	1418.03	3.65
1443.27	2.13	1487.49	0.01	1488.14	7.27
1490.85	2.79	1495.94	14.53	1502.94	7.49
1508.07	5.06	1544.88	27.13	1610.78	0.43
1653.78	0.37	3012.8	14.39	3017.69	27.96
3019.27	41.74	3021.97	31.99	3069.91	19.43
3077.35	0.02	3083.89	85.33	3090.03	22.32
3092.27	33.9	3097.98	18.09	3145.7	20.71
3146.83	5.65	3163.12	37.43	3167.15	5.33

Frequencies and intensities rounded off to 2 decimal points.

Table 11: Calculated frequencies and IR intensities of thymol from B3LYP/6-31++G(d,p) calculations

Freq. (cm^{-1})	IR int. (a.u.)	Freq. (cm^{-1})	IR int. (a.u.)	Freq. (cm^{-1})	IR int. (a.u.)
26.29	0.2	45.63	0.01	89.41	1.42
184.14	1.08	216.48	0.57	220.08	0.56
248.49	0.37	273.59	0.15	285.46	2.07
314.33	1.17	332.3	93.51	394.97	7.73
420.0	2.98	471.99	3.67	506.78	3.39
522.26	0.93	583.03	12.56	607.17	6.26
695.53	1.23	744.38	0.44	751.51	4.18
822.16	34.54	850.44	8.42	891.48	0.93
932.62	0.89	956.91	0.78	960.3	17.21
967.8	2.9	1024.79	0.07	1059.41	5.31
1083.58	8.72	1105.3	22.62	1131.58	24.86
1173.55	65.1	1188.48	13.63	1197.28	35.26
1234.85	27.11	1295.69	27.84	1320.48	47.62
1339.55	1.13	1352.83	8.55	1386.31	5.3
1401.6	6.09	1419.09	0.53	1421.75	3.79
1451.38	51.63	1491.48	8.28	1492.66	1.83
1495.47	8.04	1499.71	22.97	1510.92	8.96
1515.86	5.51	1554.57	24.15	1624.21	21.98
1664.87	34.76	3028.68	38.49	3031.42	43.84
3034.45	31.67	3047.03	4.81	3086.4	19.12
3092.9	5.93	3101.06	77.07	3107.96	33.5
3117.46	16.87	3119.47	23.45	3143.79	24.62
3178.34	12.46	3201.66	14.63	3831.08	51.41

Frequencies and intensities rounded off to 2 decimal points.

Table 12: Calculated frequencies and IR intensities of thymol from B3LYP/6-311++G(d,p) calculations

Freq. (cm^{-1})	IR int. (a.u.)	Freq. (cm^{-1})	IR int. (a.u.)	Freq. (cm^{-1})	IR int. (a.u.)
23.08	0.13	47.27	0.02	88.87	1.56
183.99	1.08	213.94	1.06	219.75	1.36
246.37	0.61	270.89	0.14	285.0	3.59
310.9	73.63	314.98	14.39	393.98	6.05
419.24	3.05	471.37	4.4	506.83	3.24
522.51	0.92	582.98	12.91	606.27	7.92
695.24	1.27	751.34	4.37	753.15	0.23
820.68	34.54	847.71	6.96	889.37	0.96
932.1	0.95	956.95	1.12	958.6	19.53
966.7	2.63	1022.88	0.02	1057.94	2.67
1082.34	8.13	1104.41	21.61	1130.57	25.43
1171.1	55.5	1183.5	17.99	1197.86	41.73
1232.68	28.68	1289.75	27.03	1315.87	36.9
1340.46	1.92	1344.73	15.77	1383.58	6.93
1396.87	6.84	1413.76	0.96	1416.9	3.98
1445.78	54.68	1487.12	7.18	1489.03	1.21
1491.75	6.25	1497.64	24.63	1507.14	8.85
1512.24	5.19	1548.81	24.62	1617.21	20.68
1656.76	34.93	3016.58	34.47	3020.88	45.86
3022.17	24.01	3033.88	4.49	3067.97	17.98
3075.04	4.99	3084.04	76.58	3089.67	32.01
3101.25	15.64	3101.94	23.55	3127.26	22.08
3162.25	11.37	3184.85	12.83	3836.92	56.51

Frequencies and intensities rounded off to 2 decimal points.